Theoretical Model of a Hollow Cathode Plasma for the Assessment of Insert and Keeper Lifetimes

Ioannis G. Mikellides,* Ira Katz,† Dan M. Goebel,‡ and James E. Polk§
Jet Propulsion Laboratory, California Institute of Technology, Pasadena, CA, 91109

Two theoretical models have been developed to aid the design of hollow cathodes that will last longer and perform better for high power (>100kW$_e$) Ion and Hall propulsion. The first, a 2D-axisymmetric, time-independent code, simulates the plasma inside the emitter region and thus depends on the measurement of at least one plasma property at the orifice entrance boundary. Simulations of the NSTAR cathode and comparisons with measurements taken inside the emitter region suggest that emission enhancement by "sheath funneling" into the insert pores is a dominant mechanism in cathodes that operate at high plasma densities (>5×10^{20} m^{-3}). It is found that most of the net electron flow in the NSTAR cathode originates from within a few millimeters of the insert edge nearest to the orifice plate. Due to the order-of-magnitude smaller peak plasma densities attained in the larger-size NEXIS cathode, the Debye sizes are larger and sheath funneling does not affect the emission characteristics significantly. The second theoretical model, a 2D-axisymmetric, time-dependent code, simulates the plasma and neutral gas dynamics in the emitter, orifice, keeper and plume regions and is more advanced in the physics and numerical approach. The time-dependent code reproduces the results of the time-independent code inside the emitter region of the NEXIS cathode at the same total pressure thus lifting all dependencies of the model on plasma measurements. Simulations using classical transport show that the electron drift velocity outside the orifice, in the near-plume region, is several times $(kT_e/m_e)^{1/2}$. The high e-i relative drifts can lead to large growth rate Buneman instabilities that can quench quickly into ion acoustic unstable modes. The finding supports previous hypotheses (made using the 2D time-independent code) of weak turbulence taking place near the orifice entrance where the electron drift was found to be only a fraction $(kT_e/m_e)^{1/2}$ but the electron temperature was several times the ion temperature.

I. Introduction

HOLLOW cathode failure is one of the most critical obstacles the electric propulsion community must overcome before establishing Ion and/or Hall as the propulsion technologies of choice for NASA's high-power, long-duration missions. Many missions considered under Project Prometheus for example would require more than ten years of continuous thruster operation. The longest operation of a hollow cathode in an electric propulsion application was achieved during the Extended Life Test (ELT) of the NASA Solar Electric Propulsion Technology Applications Readiness (NSTAR) engine in which the discharge cathode continued to operate after 30,352 hrs.[1] However, the cathode keeper had completely eroded and post-ELT analyses suggested that cathode failure would be the most likely near-term cause for the failure of the engine.[2]

The complexity associated with the physics of the multi-component fluid inside the cathode, and the difficulty of accessing empirically this region, have limited our ability to design cathodes that perform better and last longer. The

* Member Technical Staff, Advanced Propulsion Technology Group, 4800 Oak Grove Drive, Pasadena, CA, 91109, Mail Stop 125-109, Member AIAA.
† Group Supervisor, Advanced Propulsion Technology Group, 4800 Oak Grove Drive, Pasadena, CA, 91109, Mail Stop 125-109, Senior Member AIAA.
‡ Section Staff, Thermal and Propulsion Engineering Section, 4800 Oak Grove Drive, Pasadena, CA, 91109, Mail Stop 125-109, Senior Member AIAA.
§ Section Staff, Thermal and Propulsion Engineering Section, 4800 Oak Grove Drive, Pasadena, CA, 91109, Mail Stop 125-109, Member AIAA.

most prominent experimental efforts to measure the plasma properties inside and outside hollow cathodes was reported by Siegfried and Wilbur[3] in 1978 and more recently by Goebel *et al*. (2004).[4] Both studies showed that plasma densities may reach 10^{20} m^{-3} near the orifice. In the NSTAR cathode the plasma density in this region can exceed 10^{21} m^{-3}.[5] These empirical studies provided profiles of the plasma parameters by probing the region inside the cathode along the axis of symmetry, but provided no data of ion fluxes and sheath potentials off-axis. In the absence of this information the life of the emitter can not be accurately assessed. The mechanisms that degrade the life of the cathode keeper are also not well understood. Kameyama and Wilbur[6,7] proposed that a "potential hill" is created as a result of extensive electron-impact ionization during which electrons thermalize and escape quickly while ions tend to accumulate. It was proposed that this "potential hill" may responsible for the production of high-energy ions in the near-plume regions, which could then be directed by the local electric field towards the keeper. Recent measurements made by Goebel *et al*.[4,5] however, in the keeper regions of the 1.5-cm diameter hollow cathode used in the Nuclear Electric Xenon Ion System (NEXIS), and of the NSTAR cathode (0.25-in), show no potential hills; the plasma potential exhibits a monotonic increase downstream of the orifice. In the NEXIS cathode the electron temperature also continued to increase with distance from the near-plume region. Moreover, measurements in the plume region of the NSTAR cathode show oscillatory activity in the plasma, on the ion acoustic frequency scales, with higher energy ions produced off-axis than along the axis of symmetry.

The inherent two-dimensionality of the plasma both inside and outside the orificed cathode leaves (at best) little hope that 0D and 1D theoretical models can provide the understanding necessary for the identification, quantification and mitigation of the mechanisms that determine cathode life. Inside the cathode, 2D models that do not account for the coupling that exists between the plasma and the emission characteristics along the insert boundary, assume uniform electron temperature, and/or do not account for all the dominant particle collision physics (such as ion-neutral collisions) are also insufficient in determining the extent to which the emitter is utilized, and ultimately its life. Based on recent modeling by Mikellides *et al*.,[8] the physical processes that occur inside the orifice channel and conical regions strongly influence the way the plasma evolves in the near-plume region. Thus, de-coupling the two regions to simulate the plume separately would automatically force a dependence of the solution on the assumed boundary conditions, and as a consequence, the sensitivity of the solution on the choice of boundary conditions would be in question. The possible existence of non-classical heating in the orifice and near-plume regions also require that the appropriate terms representing these physics appear in the conservation laws which may include anomalous resistivity and time-dependence. Also, the long thermal equilibration times between electrons and ions imply that ions remain cold relative to the electrons in the near-plume region which means that a separate energy equation must be solved for the heavy species. Capturing the electron-to-ion temperature ratio (T_e/T_i) is critical because it strongly determines the level of damping one would expect in many mechanisms that promote wave growth.

We report here for the first time on the status of the development of the 2D-axisymmetric, time-dependent, Orificed Cathode (OrCa2D) computer code at the Jet Propulsion Laboratory (JPL), and on recent findings produced by the most recent version of the code. OrCa2D is a global theoretical model of the hollow cathode that unifies the emitter, orifice and plume regions, in two dimensions. It is a descendent of the IROrCa2D code (Insert Region of an Orificed Cathode), a 2D-axisymmetric time-independent computational model of the emitter region only. IROrCa2D was developed last year at JPL to assess life-limiting mechanisms associated with the emitter. Each code has been developed with specific objectives in mind. IROrCa2D is less demanding of computational resources than OrCa2D, less complex, and simulates a geometrically simple region namely the rectangular emitter region. The confirmation of the physics included in this first model has therefore been crucial because, once validated, IROrCa2D would lay the foundation for the development of the more ambitious OrCa2D. Therefore, although IROrCa2D results compared well with measurements of the plasma density, potential and electron temperature inside the NEXIS cathode last year, further validation of the code is pursued here with comparisons between model results and data taken inside the NSTAR cathode.

II. Theoretical Models

A. The 2D-Axisymmetric Time-Independent Code IROrCa2D

The main motivation for developing IROrCa2D last year was to identify and quantify the mechanisms that affect the life of the emitter. The objective was to develop a theoretical model that predicts the steady-state, two-dimensional distributions of all pertinent plasma properties, including electron/ion fluxes as well as the sheath potential drop along the emitter. The geometrical simplicity of the emitter region (Fig 1) allowed us to focus on the development and validation of the complex physics associated with the neutral and ionized gases inside the cathode, in the presence of electron emission from the insert boundary. The absence of time-dependent terms in the plasma

conservation equations, and the neglect of neutral gas dynamics also simplified the numerical approach and reduced the computational times required to attain the steady-state solution. The self and applied magnetic fields have also been neglected.

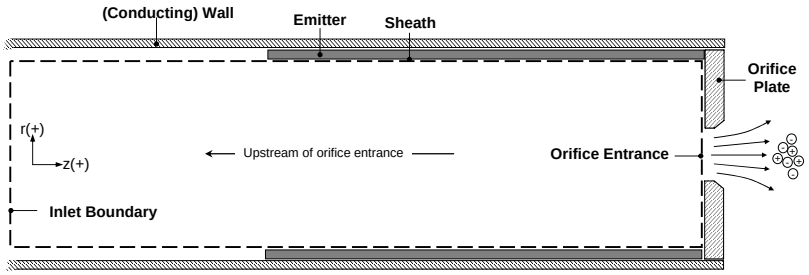

Fig 1. Schematic of the hollow cathode emitter region showing the IROrCa2D computational region (dashed line).

1. Governing equations

The governing conservation laws of IROrCa2D have been in derived in Ref 8. The final form of the system of equations solved in IROrCa2D is repeated below for completeness. The electron and ion momentum equations, in the absence of the inertia terms, are added to yield an expression for the ion current density, $\mathbf{j}_i$, as given by eqn (1) below. The electron and heavy species masses are denoted by m_e and m, respectively. The collision frequencies between electrons and neutrals, ν_{en}, between ions and neutrals, ν_{in}, and the ionization frequency ν_{iz}, have also been provided in Ref 8. Equation (1) is substituted into the ion continuity eqn (2) which is solved for the plasma density, n, with $\dot{n}$ denoting the ionization rate. Conservation of energy for the electrons is expressed by eqn (3) and yields the electron temperature T_e (in eV), with $\mathbf{E}$ and $\mathbf{j}_e$ denoting the electric field and electron current density, respectively. Loss of electron energy by ionization (inelastic) collisions is expressed by the last term in eqn (3) with ε being the first ionization potential of xenon (12.13 eV). In addition to thermal conduction using the classical electron thermal conductivity κ_e for singly ionized plasma (in W/m/eV), eqn (3) also includes the energy exchange per unit time between electrons at T_e (in K) and heavy species at T (in K) with ν_{ei} being the electron-ion collision frequency. By assuming that ions and neutrals are in thermal equilibrium, a single equation is derived for the conservation of energy of the heavy species (eqn (4)). Since the neutral dynamics are neglected in IROrCa2D (u_n=0), the heating term due to charge-exchange collisions $nm\nu_{in}u_i^2$ includes only the ion velocity u_i. The thermal conductivity for the neutral atoms is given by κ_n (in W/m/eV). Subtraction of the electron continuity equation $e^{-1}\nabla\cdot\mathbf{j}_e=-\dot{n}$ from the ion continuity equation (2) yields the statement for the conservation of total current $\nabla\cdot(\mathbf{j}_e+\mathbf{j}_i)=0$ which is combined with the electron momentum equation (6) and $E=-\nabla\phi$ to yield eqn (5) below, where η is the classical plasma resistivity. Equation (5) is solved for the plasma potential ϕ. Assuming uniform total pressure p_g throughout the cathode channel, the neutral particle density is determined using the ideal gas law, $n_n=p_n/kT$, taking into account the partial pressure from electrons and ions: $n_n=p_g/kT-n(1+T_e/T)$. The system of eight equations (six below, $E=-\nabla\phi$ and $n_n=p_g/kT-n(1+T_e/T)$), along with appropriate boundary conditions (discussed in the next section), yields the 2D profiles of n, $\mathbf{j}_i$, $\mathbf{j}_e$, $\mathbf{E}$, T_e, T, n_n and ϕ.

$$\mathbf{j}_i=\frac{m_e}{m}\frac{\nu_{en}}{\nu_{in}(1+\bar{\nu})}\mathbf{j}_e-\frac{e\nabla(nkT+nkT_e)}{m\nu_{in}(1+\bar{\nu})},\qquad \bar{\nu}\equiv\frac{\nu_{iz}}{\nu_{in}} \tag{1}$$

$$e^{-1}\nabla\cdot\mathbf{j}_i=\dot{n} \tag{2}$$

$$-\nabla\cdot\left(\frac{5}{2}T_e\mathbf{j}_e+\kappa_e\nabla T_e\right)=\mathbf{E}\cdot\mathbf{j}_e-Q_T-\dot{n}e\varepsilon,\qquad Q_T\equiv 3nk\frac{m_e}{m}(\nu_{ei}+\nu_{en})(T_e-T) \tag{3}$$

$$\nabla\cdot\left[\frac{5}{2}T\mathbf{j}_i-\kappa_n\nabla T\right]-\mathbf{u}_i\cdot\nabla(neT)=nm\nu_{in}u_i^{\,2}+Q_T \tag{4}$$

$$\nabla\cdot\left(\frac{\nabla\phi}{\eta}\right)=\nabla\cdot\left[\frac{\nabla(nT_e)}{\eta n}+\left(1-\frac{\nu_{ei}}{\nu_{en}+\nu_{ei}}\right)\mathbf{j}_i\right],\quad \eta=\frac{m_e(\nu_{en}+\nu_{ei})}{ne^2} \tag{5}$$

$$\mathbf{j}_e=\frac{\mathbf{E}}{\eta}+\frac{\nabla(nT_e)}{\eta n}-\left(\frac{\nu_{ei}}{\nu_{en}+\nu_{ei}}\right)\mathbf{j}_i \tag{6}$$

2. Boundary Conditions

The boundary conditions in IROrCa2D have been described in detail in Ref 8. The most important conditions are outlined in this section, and are followed by a recent improvement on emission enhancement. The NSTAR simulations (see section III.A) show that the latter is critical in cathodes with porous emitters when the Debye length λ_D becomes smaller than the average pore diameter.

In IROrCa2D both ions and electrons are allowed to penetrate the sheath and be absorbed by the insert walls. Ions at wall boundaries are assumed to have attained the Bohm velocity. So, the ion flux normal to wall boundaries is prescribed as $n\mathbf{u}_i\cdot\hat{\mathbf{n}}\approx 0.607n\sqrt{kT_e/m}$ with $\hat{\mathbf{n}}$ denoting the normal unit vector. The absorbed electron current density follows the one-sided thermal flux assuming Boltzmann electrons: $\mathbf{j}_e^{ab}\cdot\hat{\mathbf{n}}=-¼en\bar{c}_e e^{-e\phi/kT_e}$.

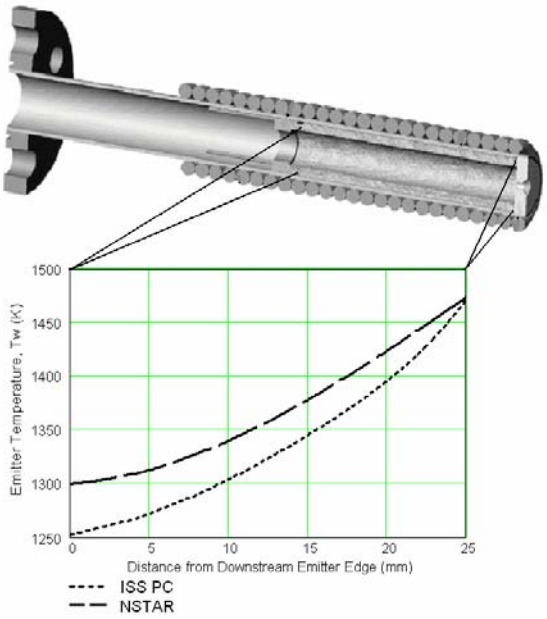

Fig 2. Temperature profiles along the emitter for the NSTAR cathode and ISS PC.

The emitted electron current density $\mathbf{j}_e^{em}$ from the insert is modeled after the Richardson-Dushman equation (7) for thermionic emission,[9] and includes the effect of the Schottky potential ϕ_{SH}.

$$\mathbf{j}_e^{em}\cdot\hat{\mathbf{n}}=\alpha T_w^{\,2}\exp\left[-\frac{e(\phi_{WF}-\phi_{SH})}{kT_w}\right] \tag{7}$$

The emitter temperature T_w (K) as a function of distance from the downstream emitter edge is prescribed by a polynomial fit to measurements, and is plotted in Fig 2 for the NSTAR cathode and for the International Space Station Plasma Contactor (ISS PC).[10] For all NSTAR simulations the work function ϕ_{WF} (V) as a function of T_w (K) is given by eqn (8) and is taken from J.L. Cronin:[11]

$$\phi_{WF}=1.67+2.82\times10^{-4}T_w \tag{8}$$

At the time the NEXIS cathode calculations were performed the emitter temperature was unknown. Thus, the variation in temperature measured for the International Space Station Plasma Contactor (ISS PC) emitter (Fig 2) was prescribed during the simulations. However, the peak temperature was varied until the discharge current requirement (nominally 25A for NEXIS) was satisfied. The details of the iterative process for determining the temperature in simulations for which the emitter temperature is unknown is described in greater detail in the following section.

A model improvement proven critical by the NSTAR simulations with IROrCa2D is emission enhancement under high plasma density conditions. The mechanism may be best characterized as "sheath funneling" and is depicted by the schematic in Fig 3. In cathodes where the plasma density is high enough so that the Debye length becomes smaller than the mean pore radius r_p, it is hypothesized that the sheath can be funneled into the pores thereby enhancing the effective emission area. This increase in area is modeled by assuming that the pores are cylinders with radius r_p and that the sheath penetrates the cylinder a distance h from the pore entrance. The penetration height h is approximated by assuming that the (collisionless) ions enter the pore along straight-line trajectories with an axial velocity component that equals the Bohm speed $(kT_e/m)^{1/2}$ and a radial component that equals the ion thermal speed $(kT/m)^{1/2}$. Then the ratio of ion particle densities $n_i(x_3=0)$ and $n_i(x_3=h)$ may be expressed by eqn (9) as follows:

$$\frac{n_i(0)}{n_i(h)} = \left(1+\sqrt{\frac{T}{T_e}}\frac{h}{r_p}\right)^2 = \frac{\lambda_D(h)^2}{\lambda_D(0)^2} \tag{9}$$

Assuming that $\lambda_D(h)=r_p$ the height h is given by,

$$\frac{h}{r_p} = \sqrt{\frac{T_e}{T}}(a-1), \qquad a \equiv \frac{r_p}{\lambda_D(0)} \tag{10}$$

To account for the enhancement, the emitted electron density $\mathbf{j}_e^{em}$ is multiplied by an emission enhancement factor f when a at any location on the emitter exceeds one. Based on the assumed geometry of the pores the factor f is easily derived as,

$$f = 1+2b\frac{h}{r_p} = 1+2b\sqrt{\frac{T_e}{T}}(\alpha-1), \qquad b \equiv \frac{A_p}{A_{em}} \tag{11}$$

where b is the ratio of open area (i.e. the sum of all pore entrance areas) over the total emitter surface area. It is approximated that for the porous emitters used in the NSTAR and NEXIS cathodes b may vary between 0.2 and 0.5 assuming a pore diameter range of 1-7 μm.[11]

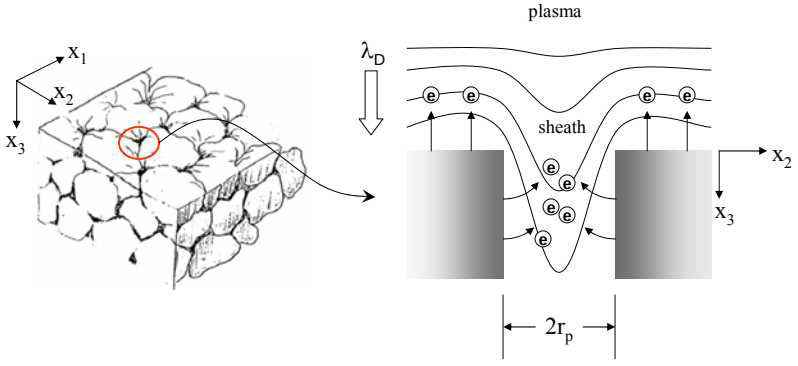

Fig 3. Left: 3D schematic of a microscopic section of the porous emitter (by R.T. Longo[12]). Right: 2D schematic of sheath funneling.

3. Numerical Approach

Since the computational region in IROrCa2D ends at the orifice entrance (which is part of the main plasma flow) conditions at this boundary must be specified. The code has been designed to require two scalar quantities at this boundary if the emitter temperature is unknown: the plasma potential and number density. These values must be provided by direct measurement. If the emitter temperature is unknown the emitter peak temperature is in fact computed by iteration until the total current out of the orifice boundary equals the current operating condition for the simulated cathode. The temperature variation along the emitter is assumed. A second simulation scenario may exist in which the emitter temperature is known from direct measurement (as in the NSTAR cathode and ISS PC). In this case the plasma potential boundary condition at the orifice is varied by iteration until the total current operating condition is satisfied. Since the neutral gas dynamics are assumed negligible inside the emitter region the mass flow rate is not specified directly in IROrCa2D. Instead, the total pressure p_g inside the cathode is specified based on direct measurement.

The conservation equations are discretized using a finite volume approach. All fluxes are edge-centered and scalars are cell-centered quantities. The fluxes are determined using second-order accurate finite differences. The system of equations is solved in a time-split manner using explicit time-marching for the plasma density and electron temperature. Initial estimates of the electron current density vector field, plasma density and electron temperature are used to compute all required fluxes, transport coefficients and related quantities. Equations (2) and (3) are then time-marched to yield new values of n and T_e. The evolution of these equations at fixed current density is repeated for N iterations. When N reaches a user-specified number, eqn (5) is solved implicitly to determine a new value of the electric potential, ϕ, which is in turn used to compute a new electric field ($\mathbf{E}=-\nabla\phi$). The electron current density vector field is then updated using the electron momentum equation (eqn (6)). Concurrently, eqn (4) is solved implicitly to determine the new heavy species temperature, T. The procedure is repeated until the solution for all quantities has reached steady state.

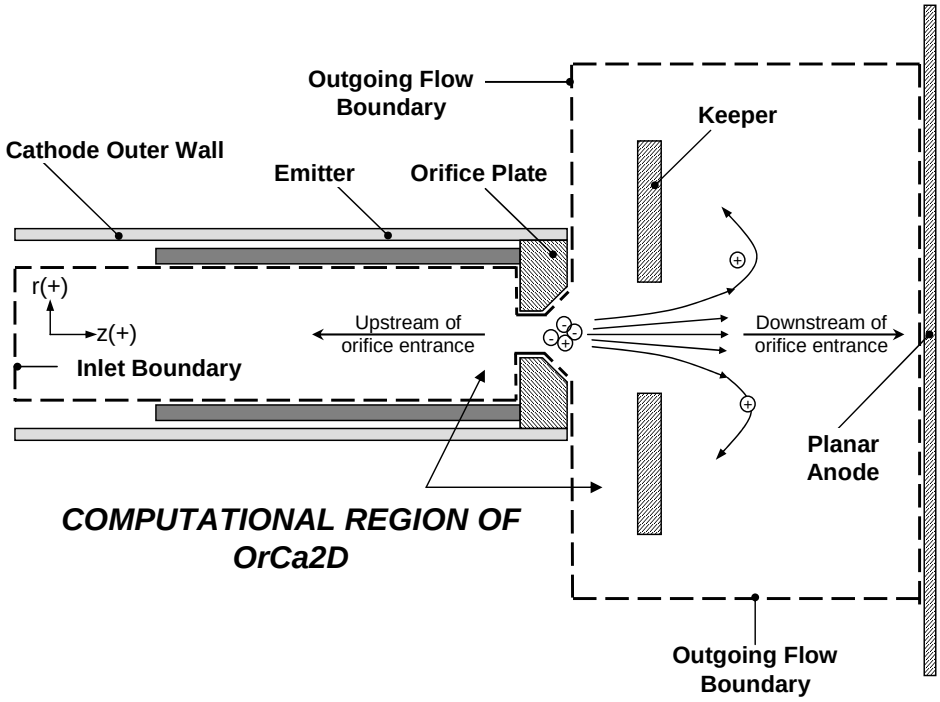

Fig 4. Schematic of the hollow cathode emitter, orifice and plume regions showing the OrCa2D computational region (dashed line).

B. The 2D-Axisymmetric Time-Dependent Code OrCa2D

Although a descendent of IROrCa2D, OrCa2D is a major advancement over IROrCa2D both in the physics and numerics. The main motivation behind the development of OrCa2D is the assessment of keeper erosion and lifetime. Thus, in addition to the insert region the computational region in OrCa2D includes the orifice channel and conical regions as well as the keeper and plume regions (Fig 4). The plume region extends up to an anode boundary several

centimeters downstream of the orifice. Since the assumption of uniform total pressure is not valid in the orifice and plume regions OrCa2D includes neutral gas dynamics. Past simulations of the NEXIS insert region using IROrCa2D suggested that anomalous transport due to oscillations involving the heavy species may be responsible for the heating and high potential gradients measured near the orifice and near-field plume regions. Being a time-independent code with a computational region that ends at the orifice entrance, it is not possible to assess such mechanisms with IROrCa2D. Thus, OrCa2D is being developed to include all time-dependent terms that may be pertinent to ion acoustic and/or ionization oscillations. Currently, all time-dependent terms have been included in OrCa2D except for ion inertia which is planned for the very near future. The magnetic field is also excluded from the present version. With ion acceleration physics it will be possible to quantify the ion energies in the keeper region and the mechanisms that cause them. By extending the computational region to include the anode boundary and by including neutral gas dynamics, OrCa2D is a self-reliant code that requires knowledge of the cathode operating conditions (such as mass flow rate and discharge current) and emitter temperature but does not depend on experimental measurements of any of the plasma properties.

As a consequence of including time-dependence several numerical advancements had to be made in OrCa2D over IROrCa2D. In short, all conservation laws for the plasma have been strongly implicitized in OrCa2D to improve computational time and to eliminate numerical oscillations associated with most explicit schemes. Only the neutral gas continuity and momentum equations are solved explicitly since their time scales are very long compared to the plasma time scales. With the presence of the momentum convection terms (inertia) in the neutral momentum equation, a Riemann solver has been incorporated that is based on Gudonov's 1st order accurate upwind scheme. A predictor-corrector has also been incorporated in the solution of the neutral gas continuity and momentum to smooth out numerical instabilities.

1. Governing equations

The system of conservation laws in OrCa2D is presented below in the sequence it is solved numerically. Noted are the time-dependent terms in the ion continuity (eqn (14)) and electron energy laws (eqn (15)). Also noted are the neutral continuity (eqn (19)) and momentum laws (eqn (18)) none of which appear in IROrCa2D system. The neutral particle flux $(n\mathbf{u})_n$ is denoted by $\mathbf{\Gamma}_n$. Time-dependence has not yet been implemented in eqn (12) but the collision term due to the presence of non-zero neutral velocities has been included. As in IROrCa2D, the heavy-species energy equation assumes that the ions and neutrals are in thermal equilibrium but the presence of neutral dynamics requires the additional terms that appear in eqn (20) involving the neutral particle velocity $\mathbf{u}_n$.

Plasma

$$\mathbf{j}_i = \frac{m_e}{m}\frac{\nu_{en}}{\nu_{in}(1+\bar{\nu})}\mathbf{j}_e - \frac{e\nabla(nkT + nkT_e)}{m\nu_{in}(1+\bar{\nu})} + \frac{en\mathbf{u}_n}{(1+\bar{\nu})} \tag{12}$$

$$\mathbf{E} = \eta\mathbf{j}_e - \frac{\nabla(nT_e)}{n} + \frac{m_e\nu_{ei}}{e^2 n}\mathbf{j}_i \tag{13}$$

$$\frac{\partial n}{\partial t} + e^{-1}\nabla\cdot\mathbf{j}_i = \dot{n} \tag{14}$$

$$\frac{3}{2}en\frac{\partial T_e}{\partial t} = \mathbf{E}\cdot\mathbf{j}_e + \nabla\cdot\left(\frac{5}{2}T_e\mathbf{j}_e + \kappa_e\nabla T_e\right) + \frac{3}{2}T_e\nabla\cdot\mathbf{j}_i - e\dot{n}\left(\varepsilon + \frac{3}{2}T_e\right) - Q_T \tag{15}$$

$$\nabla\cdot(\mathbf{j}_e + \mathbf{j}_i) = 0 \rightarrow \nabla\cdot\left(\frac{\nabla\phi}{\eta}\right) = \nabla\cdot\left[\frac{\nabla(nT_e)}{\eta n} + \left(1 - \frac{\nu_{ei}}{\nu_{en}+\nu_{ei}}\right)\mathbf{j}_i\right] \tag{16}$$

$$\mathbf{j}_e = -\frac{\nabla\phi}{\eta} + \frac{\nabla(nT_e)}{\eta n} - \left(\frac{\nu_{ei}}{\nu_{en}+\nu_{ei}}\right)\mathbf{j}_i \tag{17}$$

Neutral Gas

$$\frac{\partial \boldsymbol{\Gamma}_n}{\partial t} + \nabla \cdot \left(\boldsymbol{\Gamma}\mathbf{u}\right)_n = n\nu_{in}\left(\mathbf{u}_i - \mathbf{u}_n\right) - \frac{\nabla\left(n_n kT\right)}{m} \tag{18}$$

$$\frac{\partial n_n}{\partial t} + \nabla \cdot \boldsymbol{\Gamma}_n = -\dot{n} \tag{19}$$

$$\begin{aligned} \frac{3}{2}e\left(n_n + n\right)\frac{\partial T}{\partial t} = nm\nu_{in}\left(\mathbf{u}_i - \mathbf{u}_n\right)^2 - \nabla \cdot \left[\frac{3}{2}T\left(\mathbf{j}_i + e\boldsymbol{\Gamma}_n\right) - \kappa_n \nabla T\right] \\ -eT\left[n\nabla \cdot \mathbf{u}_i + n_n \nabla \cdot \mathbf{u}_n\right] + \frac{3}{2}T\left[\nabla \cdot \left(\mathbf{j}_i + e\boldsymbol{\Gamma}_n\right)\right] \end{aligned} \tag{20}$$

2. Boundary Conditions

Conditions at several additional boundaries are required in OrCa2D compared to IrOrCa2D. The extended computational region in OrCa2D includes the orifice channel walls, keeper walls, free-flow boundaries at the end of the plume region and the anode boundary. The addition of neutral gas dynamics also requires new conditions at boundaries that exist in both IROrCa2D and OrCa2D. No changes exist between the two codes for the emitting boundary and conducting wall adjoining the emitter. The reader is referred to Ref. 8 for a detailed description of these boundary conditions.

Plasma Conditions Along the Orifice Plate and Plume Boundaries. Referring to Fig 4 the orifice plate walls include the orifice cylindrical and conical regions, and the outer plate surface. The keeper has not yet been implemented. The conditions for the ion current density, absorbed electron current density and energy fluxes are the same as those for the emitter-adjoining wall and orifice plate surface facing the insert region plasma. These conditions have been described in detail in Ref. 8. No electron emission is allowed from these surfaces. All orifice plate surface temperatures are set equal to the peak emitter temperature. The heavy-species temperature at these boundaries is set equal to the local wall temperature.

Presently it is assumed that all available current is collected by the anode. Therefore no ion and no electron fluxes are allowed out of the outgoing flow boundaries. Both the electron pressure and temperature gradients are assumed to be zero there. These assumptions are not strictly true, especially for the heavy ions, but sensitivity calculations which allowed ion flux out of these boundaries demonstrated little change in the solution. In general the far-field plume region is relatively benign so minor changes in the far-plume boundaries affect the behavior of the expanding plasma and gas in the near-orifice only slightly. The behavior inside the cathode remains unaffected.

Both OrCa2D and IROrCa2D assume that quasi-neutrality prevails in the ionized gas. Although "0-sheath thickness" boundary conditions are implemented at wall surfaces, the sheaths themselves can not be resolved due to their small scale lengths (~0.01mm in far-plume region, ~0.001mm in orifice). The anode boundary is therefore modeled as a mixed boundary. Specifically, the plasma density and potential are assumed to be uniform along the anode boundary. The plasma density is specified by a value that is not far from that of a free-expanding plasma in vacuum, and is at least three orders of magnitude less than the peak density inside the cathode. Small variations in the choice of density at this boundary have been found to affect negligibly the solution. Similarly to the approach followed for the orifice boundary in IROrCa2D, the anode plasma potential is specified upon sub-iteration of the plasma potential solver (eqn (16)) at each timestep until the desired discharge current operating condition is satisfied. This implies that the emitter temperature must be known. With the plasma potential and density specified then the anode boundary is of the same type as the orifice entrance boundary in IROrCa2D and all other required conditions including particle and energy fluxes are determined in the same manner.

Neutral Gas Boundary Conditions. A major addition in OrCa2D has been the model for the neutral gas dynamics and its accompanying boundary conditions for the neutral particle fluxes, energy fluxes and the neutral velocity. At the cathode inlet the incoming velocity u_{inl}, particle and energy fluxes of neutrals are specified as follows:

$$\mathbf{u}_n \cdot \hat{\mathbf{n}} = u_{inl}, \qquad \boldsymbol{\Gamma}_n \cdot \hat{\mathbf{n}} = \frac{\dot{m}}{mA_{inl}}, \qquad \left(eT\boldsymbol{\Gamma}\right)_n \cdot \hat{\mathbf{n}} = \frac{3}{2}\left(\frac{T_{cel} + T_{bdr}}{2}\right)\frac{e\dot{m}}{mA_{inl}} \tag{21}$$

where $\dot{m}$ is the total mass flow rate, A_{inl} is the inlet area, T_{cel} is the temperature in the computational cell adjacent to the boundary and T_{bdr} is the temperature (specified) at the boundary. The expression for the neutral flux above implies that negligible plasma exists in this region compared to neutrals which is a good assumption if the inlet is placed far enough from the orifice. The inlet velocity is currently set at 10 m/s. All wall boundaries that receive flux of ions are assumed to release that flux back into the computational region as neutrals:

$$\begin{gathered} \mathbf{u}_n \cdot \hat{\mathbf{n}} = 0, \qquad \boldsymbol{\Gamma}_n \cdot \hat{\mathbf{n}} = -e^{-1}\mathbf{j}_i \cdot \hat{\mathbf{n}} \\ \left(eT\boldsymbol{\Gamma}\right)_n \cdot \hat{\mathbf{n}} = \frac{3}{2}e\boldsymbol{\Gamma}_n \cdot \hat{\mathbf{n}}\left(T_{cel} - T_{bdr}\right) - \frac{3}{2}T_{cel}\mathbf{j}_i \cdot \hat{\mathbf{n}} = \frac{3}{2}\left(2T_{cel} - T_{bdr}\right)\mathbf{j}_i \cdot \hat{\mathbf{n}} \end{gathered} \tag{22}$$

At the outgoing flow and anode boundaries neutrals are assumed to flow outward freely at fixed velocity.

$$\hat{\mathbf{n}} \cdot \nabla \mathbf{u}_n = 0, \qquad \boldsymbol{\Gamma}_n \cdot \hat{\mathbf{n}} = n_{n,cel}\mathbf{u}_{n,edg}, \qquad \left(eT\boldsymbol{\Gamma}\right)_n \cdot \hat{\mathbf{n}} = \frac{3}{2}\left(\frac{T_{cel} + T_{bdr}}{2}\right)en_{n,cel}\mathbf{u}_{n,edg} \tag{23}$$

where $n_{n,cel}$ is the neutral particle density at the last cell adjacent to the boundary, and $u_{n,edg}$ is the neutral velocity at the last cell edge parallel to the boundary.

3. Numerical Approach

As in IROrCa2D, the conservation equations in OrCa2DD are descretized using finite volumes with all vectors defined at cell edges and all scalars defined at cell centers. But the relative straightforwardness with which terms of the type $\nabla\cdot(n\mathbf{u})$ or $\nabla\cdot(\alpha\nabla n)$ are discretized using finite volumes is no longer applicable in the neutral momentum equation due to the appearance of the velocity dyad in $\nabla\cdot(n\mathbf{uu})_n$. The descritization of the neutral momentum equation is described in greater detail later in this section.

The system of equations in OrCa2D is solved in a time-split manner for the following nine main variables: n, $\mathbf{j}_i$, $\mathbf{E}$, $\mathbf{j}_e$, T_e, T, n_n, ϕ and $\boldsymbol{\Gamma}_n$. The ion current density $\mathbf{j}_i$ is determined first from eqn (12) and the electric field follows using the electron momentum equation (13). The plasma density at t+Δt is then computed implicitly using eqn (14). The time-dependent equations can in general be written in the following form:

$$\beta\frac{\partial s}{\partial t} + \nabla\cdot\left(-\alpha\nabla s\right) + F = B \tag{24}$$

where s is the scalar variable eqn (24) is solve for, β is a constant (or another scalar variable) and α is a transport coefficient. The cell-centered quantity B on the right-hand-side includes all the residual terms produced by the implicitization and is evaluated at time t, and F is a cell-centered quantity that is linearized as shown in eqn (25b) below. For example, in the electron energy equation $F=e\dot{n}\varepsilon$ while in the ion continuity equation F=0, β=1, s=n and $\alpha \equiv e\left(T + T_e\right)/m\bar{\nu}$. In the descitization eqn (25a) below, subscripts "cel" and "nbr" denote computational cell and neighboring computational cell on the side "edg" of cell "cel". The cell volume is ΔV and C is a geometrical coefficient.

$$\begin{aligned} &\beta\frac{s_{cel}^{t+\Delta t} - s_{cel}^{t}}{\Delta t} + \frac{1}{\Delta V_{cel}}\sum_{edg=1}^{4}\left(s_{cel}^{t+\Delta t} - s_{nbr,edg}^{t+\Delta t}\right)C_{nbr,edg} + F(s_{cel}^{t+\Delta t}) = B_{cel}^{t} \qquad \text{(a)} \\ &F_{cel}^{t+\Delta t} \equiv F(s_{cel}^{t+\Delta t}) \approx F_{cel}^{t} + \left.\frac{\partial F}{\partial s}\right|_{s_{cel}^{t}}\left(s_{cel}^{t+\Delta t} - s_{cel}^{t}\right) = F_{cel}^{t} + F_s\left(s_{cel}^{t+\Delta t} - s_{cel}^{t}\right) \qquad \text{(b)} \end{aligned} \tag{25}$$

The electron energy eqn (15) is solved next with both the thermal convection and diffusion terms, $(5/2)T_e\mathbf{j}_e$ and $\kappa_e\nabla T_e$, implicitized and the ionization loss term linearized. Then, the plasma potential solver is called repeatedly during each timestep dt until the plasma potential solution and anode potential satisfy eqn (16) and the total current (I) operating condition $\iint(\mathbf{j}_e+\mathbf{j}_i)\cdot d\mathbf{A}_{and}=I$, where A_{and} is the anode collecting area. The electron current density vector field is then determined using the electron momentum equation and $E=-\nabla\phi$. Finally, once the plasma variables have been determined, the neutral particle density, flux and heavy-species temperature are computed.

The numerical approach for the neutral gas momentum equation uses an upwind finite volume scheme by applying the Godunov 1st-order upwind fluxes across each edge in the same way it is done for one-dimensional problems. The required vectors along edges are specified as the averages of the edge-centered vectors. The scheme is numerically diffusive and stable but is the least accurate compared to higher order schemes. Accuracy is improved in OrCa2D by implementing higher-order upwind biasing. No flux-limiting is presently employed. Comparisons with known solutions (such as quasi-1D nozzle expansion) show that the error is less that 2% for the density and less than 18% for the velocity. The 2D rectilinear grid used in OrCa2D introduces additional errors which become noticeable only far downstream of the orifice. Both the neutral continuity and momentum equations are evolved explicitly in time.

III. Results and Comparisons with Measurements

A. Simulation of the NSTAR Cathode with IROrCa2D

Upon its completion, the validation of IROrCa2D begun last year with comparisons between model results and measurements inside the NEXIS cathode. The model predictions were found to be in good agreement with measurements of the plasma density, plasma potential and electron temperature along the axis of symmetry.[8] The simulations also suggested the possibility of anomalous transport in the orifice region. Without an extended computational region that includes the orifice and plume regions however, the hypotheses of anomalous mechanisms could not be substantiated. This has been one of the main reasons for developing the time-dependent OrCa2D.

The validation of IROrCa2D continues here as we present comparisons between theoretical results and measurements taken in the NSTAR cathode. It is noted *apriori* that a significant difference between the two cathodes operating at nominal conditions is that the peak plasma density in the NSTAR cathode is almost one order of magnitude higher than in the NEXIS cathode. Figure 5 compares the Debye length along the emitter wall as computed by IROrCa2D. It is seen that emission enhancement is expected to be significant in the NSTAR cathode since the Debye length is as much as 2.5x smaller than the minimum average pore radius (assumed to be 1μm in this study) and as much as 7.5x the maximum pore radius (assumed to be 3μm). By contrast, the same effect is not expected to be as significant in the NEXIS cathode. For all simulations reported herein the average pore radius has been taken to be 2 μm.

Figure 6 shows a comparison between the computed and measured plasma densities along the axis of symmetry for the NSTAR nominal operating condition of 12A and 4.25 sccm. The measured (total) pressure during operation of the cathode was 7.9 Torr. The comparison suggests poor agreement without emission enhancement by sheath-funneling but the agreement is excellent if enhancement is included using b=0.5. Figure 7 shows the 2D plasma density profiles for the two cases b=0 (bottom) and b=0.5 (top). It is evident that most of the net electron flow into the orifice comes from within a few millimeters of the emitter downstream edge (z=4cm) when b=0.5. By comparison, the effect of emission enhancement for the NEXIS cathode at the same b is negligible as illustrated by Fig 8 and Fig 9. The variation of the net electron current density along the emitter in the two cathodes plotted in Fig 10 shows that the NSTAR net value can be more than 5x the NEXIS value within a few millimeters of the emitter tip. In view of the complexity associated with the micromorphology of the emitter pores it is noted that the agreement at b=0.5 and the simplicity of the formulation presented in section II.A.2 only suggests that a likely mechanism for the sharp drop in plasma density (within a few millimeters of the orifice entrance) has been identified. The agreement at b=0.5 is not meant to imply that the formulation is exact nor that the pores are perfect cylinders. The important deduction here is that the emission enhancement has a dependence on the inverse of the Debye length and thus depends on $\sim\sqrt{n}$. Thus, cathodes that employ the same type of porous emitters as NSTAR and operate at high enough plasma densities such that the Debye length becomes smaller than the mean pore radius, emission enhancement is likely, leading to poor utilization of the emitter. The agreement for the electron temperature is also good as shown in Fig 11. A minimum in T_e is predicted by the theory which occurs between $3.5\text{cm}<z<3.6\text{cm}$. As shown in Fig 10 this is the region of the cathode where the net electron current density vectors along the emitter reverse sign from net emission to net absorption causing cooling of the plasma.

The comparison for the plasma potential in the NSTAR cathode warrants further discussion. Figure 12 shows that the computed slope of the plasma potential is predicted well near the orifice. It is noted that the experimental error associated with the axial alignment of the probe is ±0.5mm. However, the slope a few millimeters upstream of the orifice entrance is predicted by IROrCa2D to be much steeper than the measured slope. Moreover, for all cases of b the computed plasma potential eventually reaches negative values beyond some location upstream of the orifice. For example in the b=0.5 case, for which the best agreement with the measured plasma density was achieved near the orifice (Fig 6), the plasma potential along the axis of symmetry becomes negative at approximately 7mm

upstream of the orifice. Along the emitter wall the potential becomes negative at about 5mm upstream of the orifice. By contrast, in the NEXIS cathode the computed and measured plasma potentials agree well and are positive throughout the region (Fig 13). As also shown in Fig 13 emission enhancement affects negligibly the plasma potential and electron temperature solutions in this cathode.

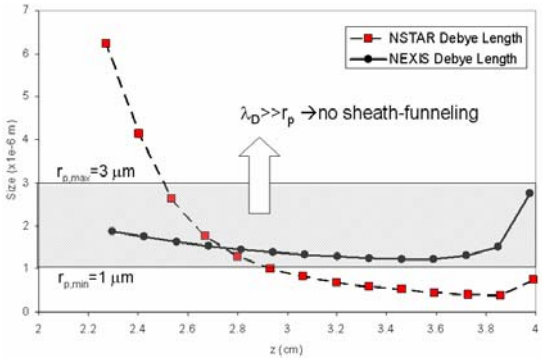

Fig 5. Comparison between the Debye length along the emitter and limiting values of the mean pore radius

A closer look at the plasma particle density comparison for b=0.5 in the NSTAR cathode on log scale (Fig 14) reveals that the computed density is in fact much higher than the measured density beyond the emission-enhanced region; the deviation begins at about 6mm upstream of the orifice, which is approximately where the plasma potential sign changes from positive to negative. The enhanced plasma densities computed by the code point to an over prediction of electron emission in this region of negative plasma potentials. Specifically, when the plasma potential along the wall becomes negative enough emitted electrons do not have sufficient energy to overcome the sheath barrier and enter the plasma, but this is has not been accounted for in the simulations up to this point. This over prediction also leads to an incorrect directionality of the $\mathbf{j}_e$ streamlines as shown in Fig 16 (top). The result with emission turn-off when the potentials become negative is shown in Fig 14 for b=0.4 and 0.5. The agreement is now much better for z<3.4 predicting very well the measured trend of an exponentially decreasing plasma density. The agreement achieved for z>3.4 is only slightly affected (as expected). With emission turn-off the electron temperature is also computed to decrease monotonically (Fig 15, left) and does not exhibit the minimum seen in the case of no emission turn-off, which is in better agreement with the measured trend.

The general distribution of the $\mathbf{j}_e$ streamlines has also changed favorably as a result of the emission turn-off correction along the emitter boundary as shown in Fig 16 (bottom). The streamlines now exhibit a trend similar to that observed in the NEXIS cathode (Fig 9) where a saddle point for the electron flow (electrons moving away from this point) is established somewhere along the axis of symmetry. However, despite this reversal of the streamlines IROrCa2D continues to over predict the electric field compared to the measurement (Fig 15, right). Interestingly, in the region 3.55cm<z<3.95cm the data suggest there is almost no electric field. In this region, using the measured plasma density and electron temperature, the e-e mean free path varies from 0.03mm to 0.15mm which implies a collisional electron flow. Thus, assuming that ions play a negligible role (which is a good approximation in this region), electrons must flow *away* from the orifice (towards the cathode inlet) since according to Ohm's Law:

$$\nabla\phi \approx -\eta \mathbf{j}_e + \frac{\nabla(nT_e)}{n} \tag{26}$$

and thus $\mathbf{j}_e(\mathbf{E}=0)\approx\nabla(nT_e)/n\eta$. Using the measured density and temperature at z=3.7cm, and assuming classical resistivity, the magnitude of the electron current density would have to be $\mathbf{j}_e(z=3.7\text{cm})=166\text{A/cm}^2$. This would also imply that the electron saddle point is located somewhere between z=3.93cm and z=4.0cm (the orifice entrance), which is more than 2mm nearer the orifice entrance than the computed saddle point location (z=3.7cm). It is noted that the computed plasma potential follows from eqn (26) in this region and is driven mostly by the electron pressure gradient since the electron current density around the saddle point is relatively small: $\mathbf{j}_e(z=3.6\text{cm})=13\text{A/cm}^2$ and $\mathbf{j}_e(z=3.8\text{cm})=-40\text{A/cm}^2$. Both the theoretical results and measurements are being re-examined to better understand the plasma potential comparison (Fig 15, right) in light of the good agreement that has been achieved in this region between theory and experiment for the plasma particle density (Fig 14) and electron temperature (Fig 15, left), as well as for all three variables in the NEXIS cathode (Fig 8 and Fig 13).

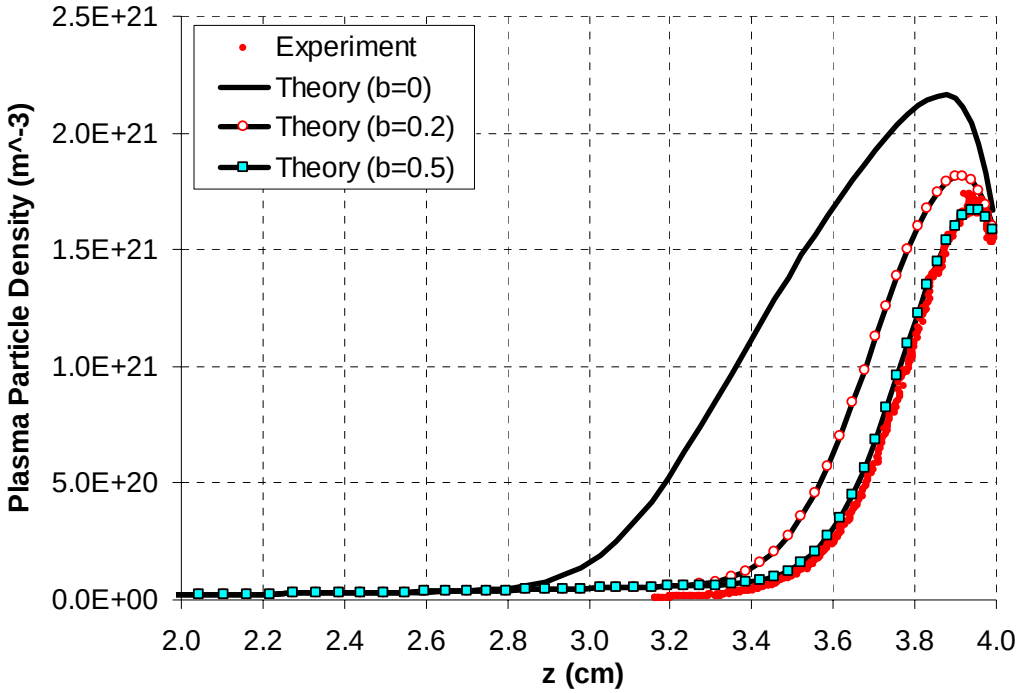

Fig 6. Comparison between measurements and theory (using the IROrCa2D code) for the plasma particle density along the axis of symmetry of the NSTAR cathode.

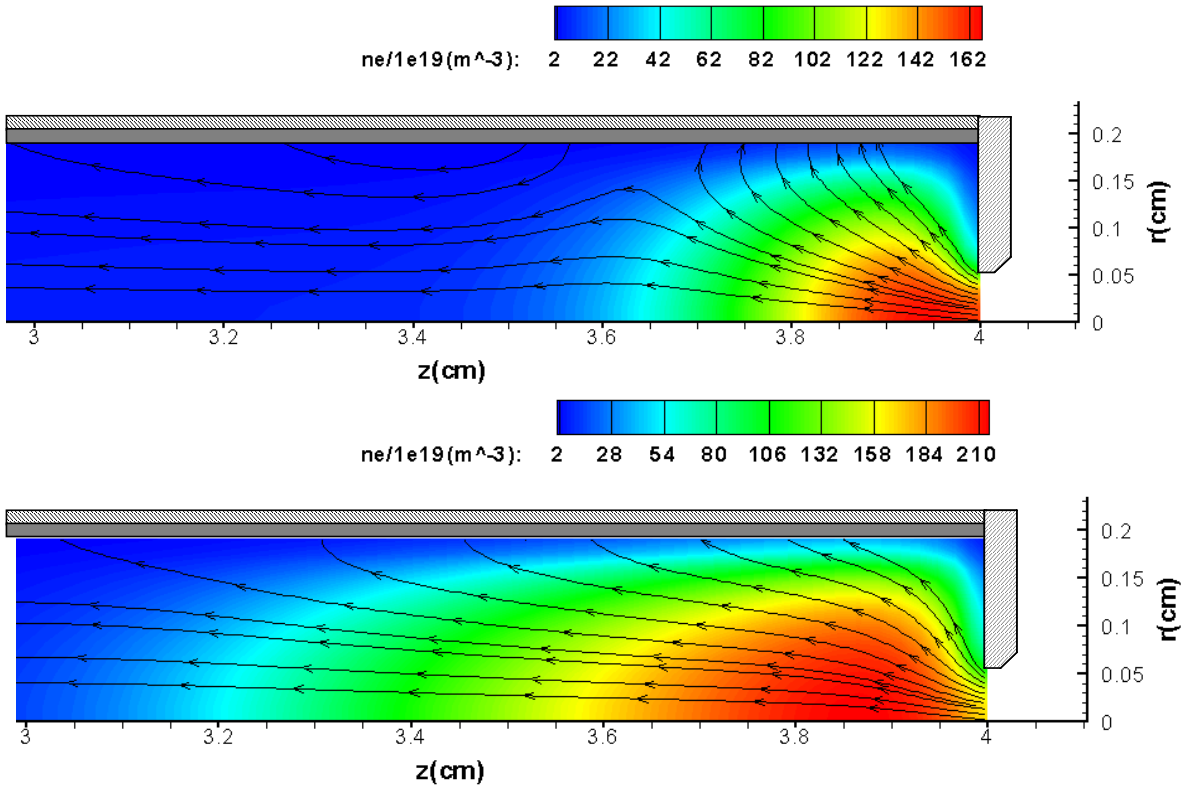

Fig 7. Computed profiles of the plasma particle density inside the NSTAR cathode overlaid by electron current density streamlines. Top: b=0.5. Bottom: b=0 (no emission enhancement).

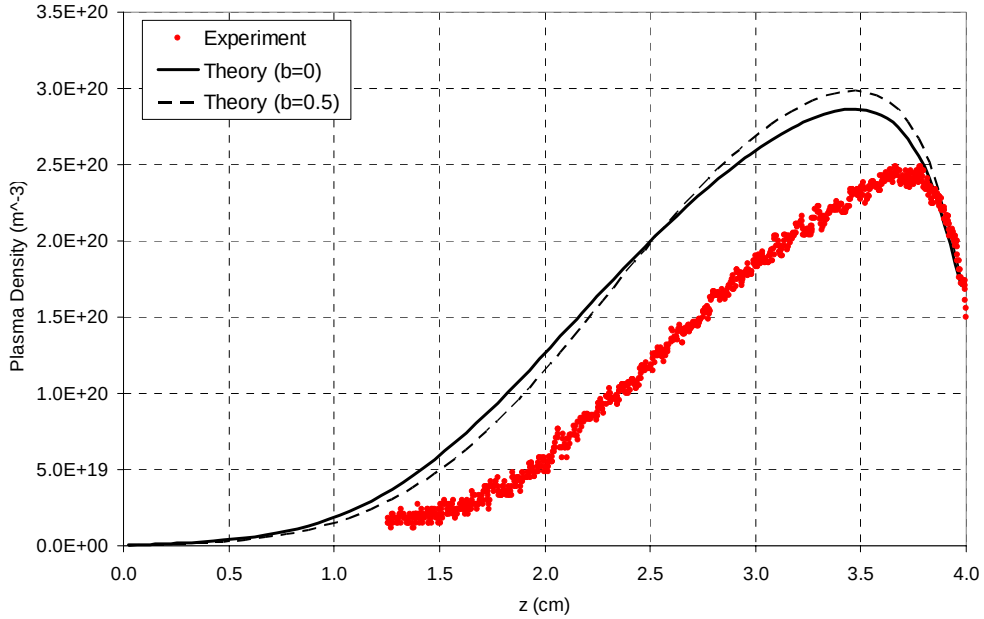

Fig 8. Comparison between measurements and theory (using the IROrCa2D code) for the plasma particle density along the axis of symmetry of the NEXIS cathode.

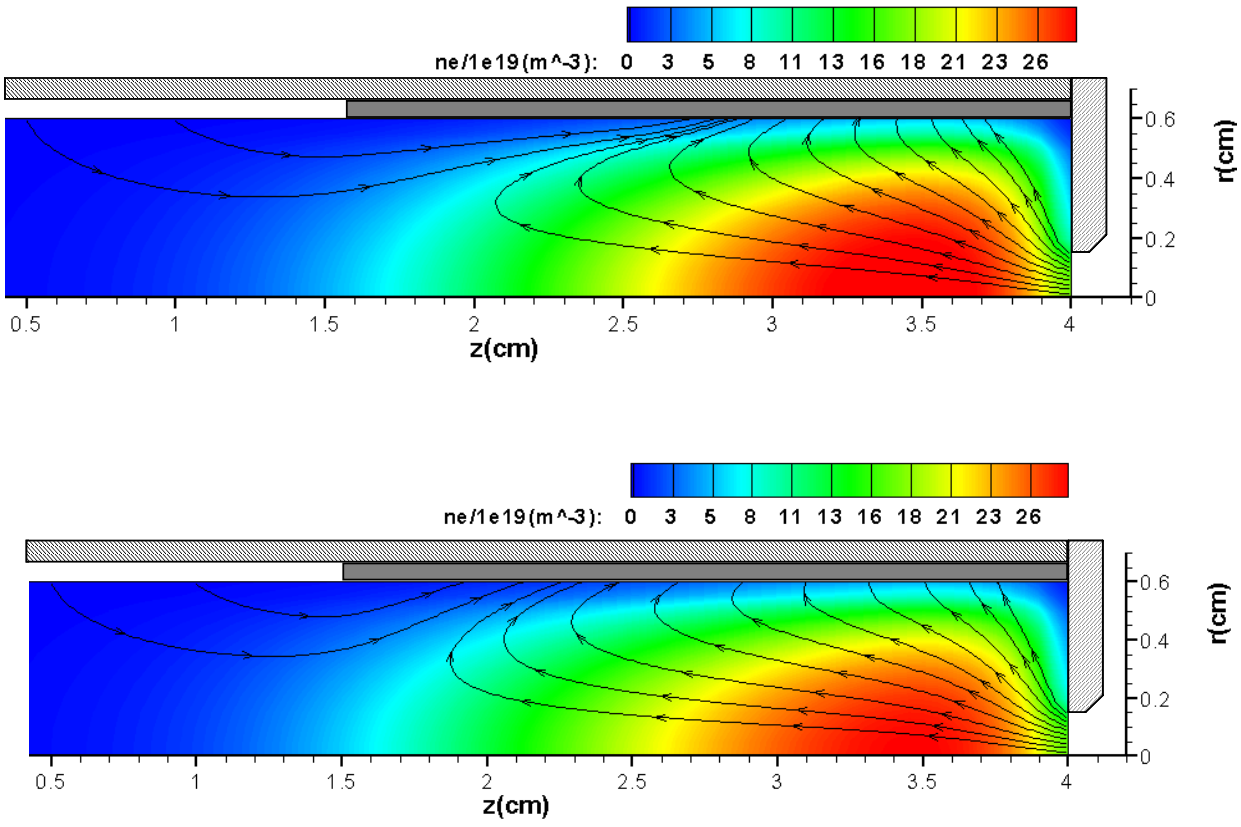

Fig 9. Computed profiles of the plasma particle density inside the NEXIS cathode overlaid by electron current density streamlines. Top: b=0.5. Bottom: b=0 (no emission enhancement).

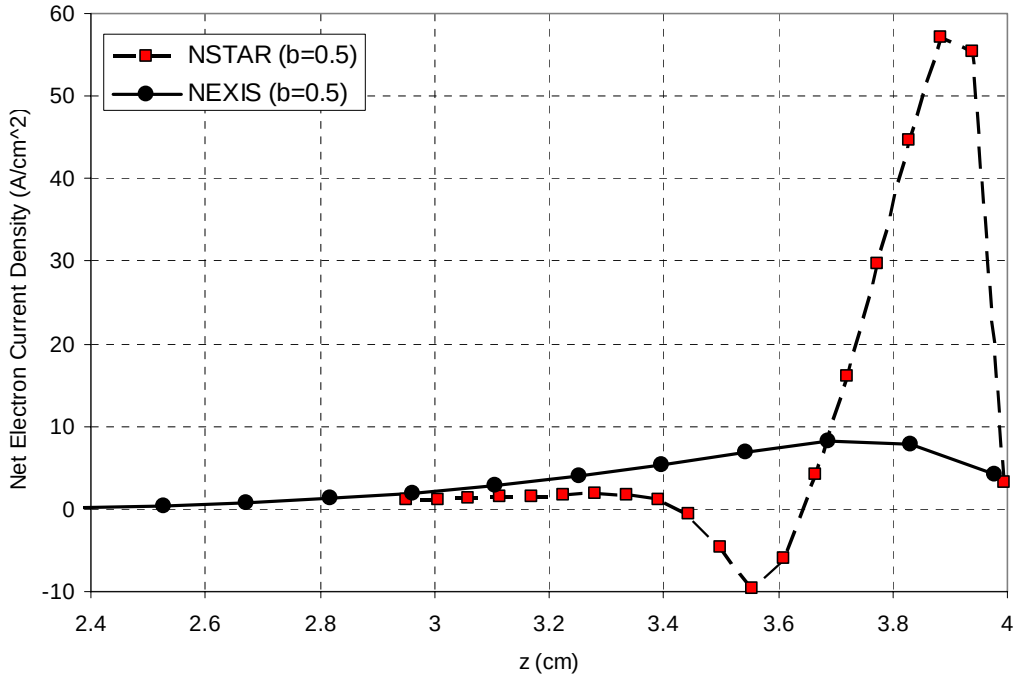

Fig 10. Comparison between the computed net electron current densities along the emitters of the NSTAR and NEXIS cathodes.

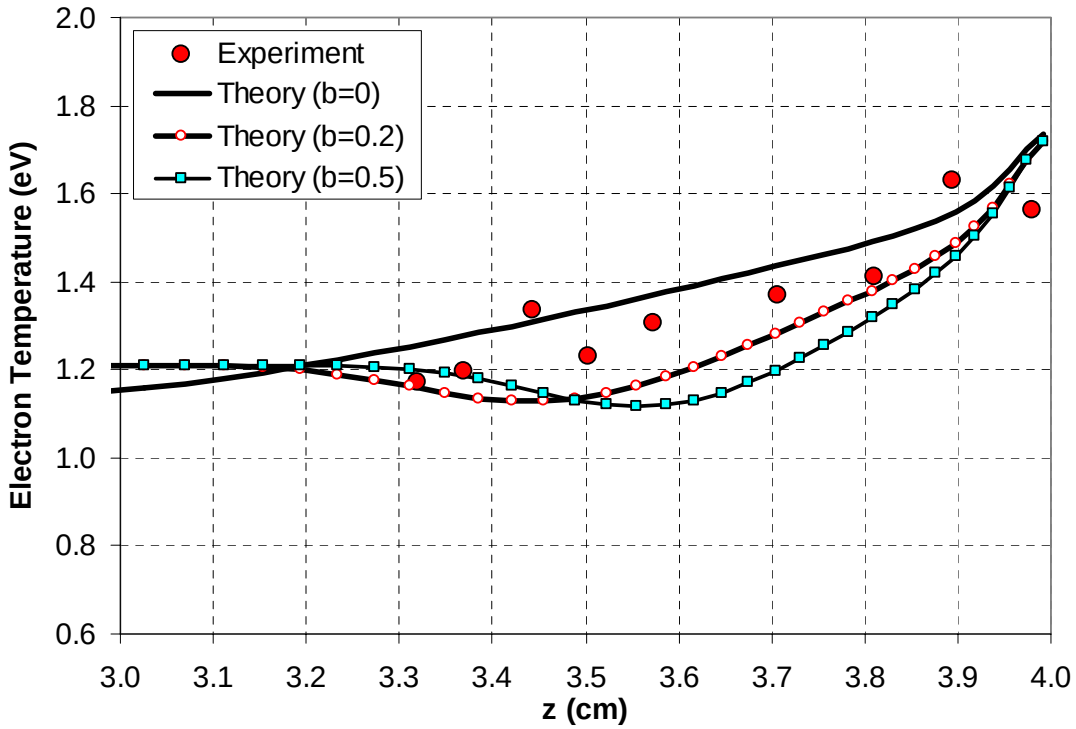

Fig 11. Comparison between measurements and theory (using the IROrCa2D code) for the electron temperature along the axis of symmetry of the NSTAR cathode.

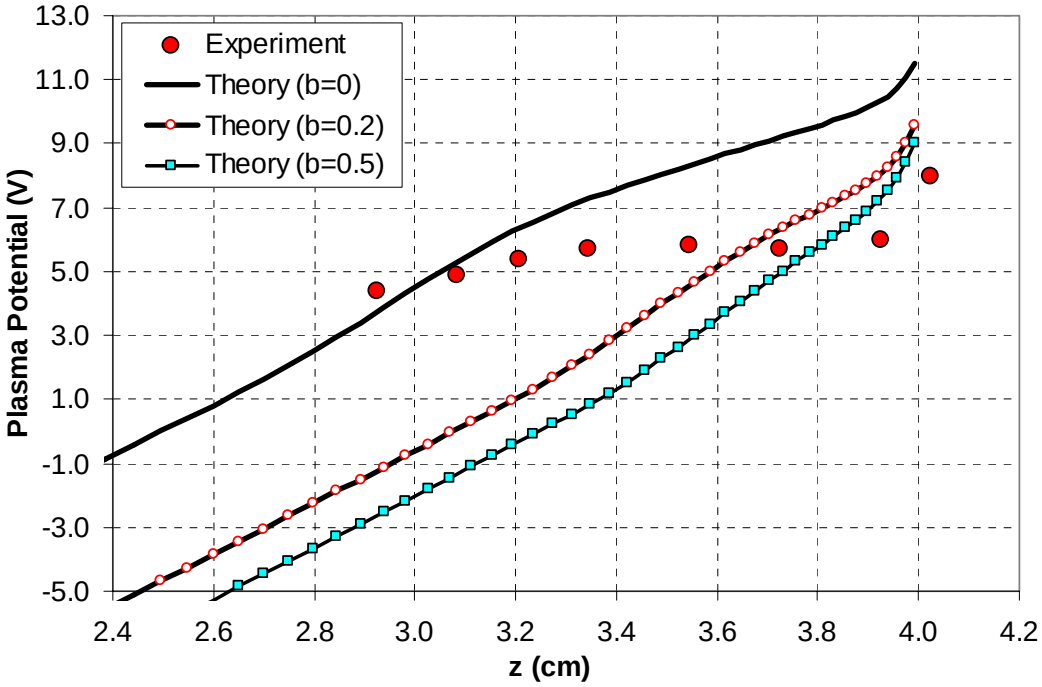

Fig 12. Comparison between measurements and theory (using the IROrCa2D code) for the plasma potential along the axis of symmetry of the NSTAR cathode.

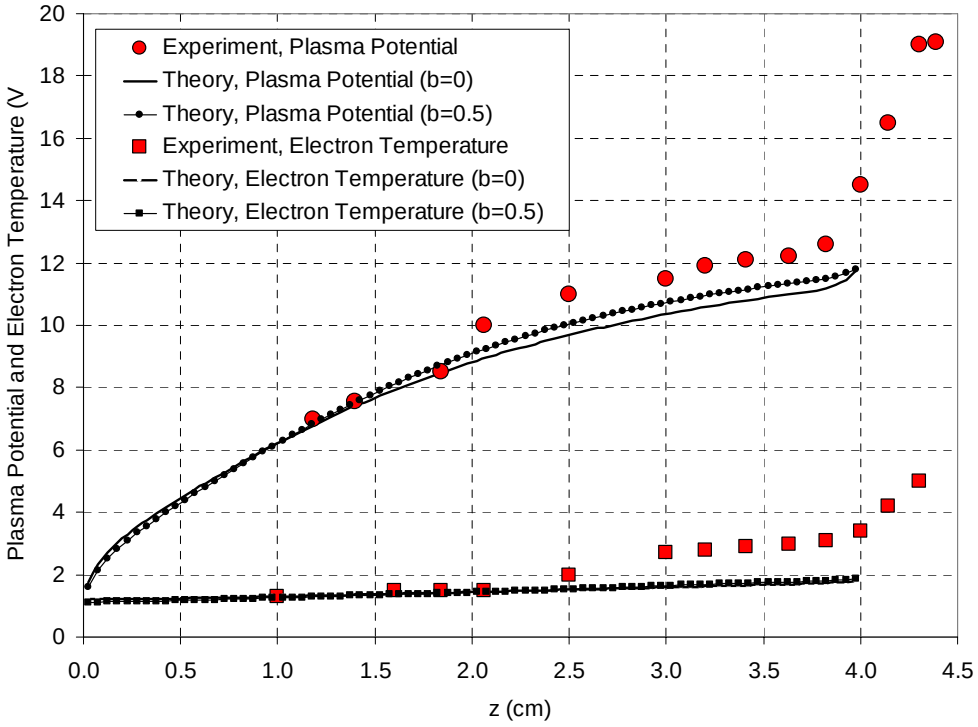

Fig 13. Comparison between measurements and theory (using the IROrCa2D code) for the plasma potential along the axis of symmetry of the NEXIS cathode.

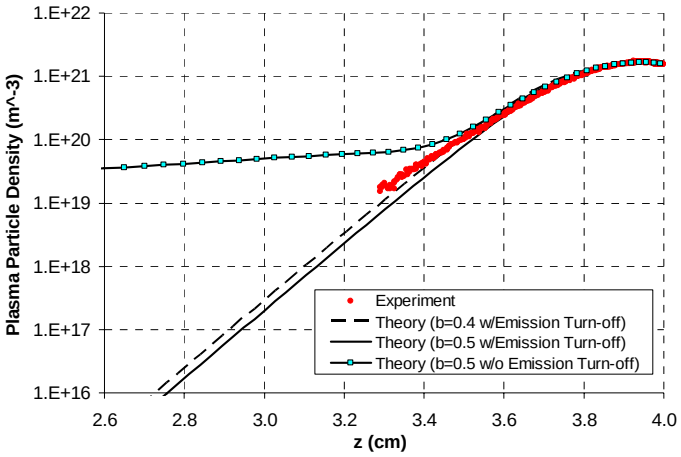

Fig 14. Comparison between measurements and theory (using the IROrCa2D code) for the plasma particle density along the axis of symmetry of the NSTAR cathode, including theory cases of emission turn-off at negative potential.

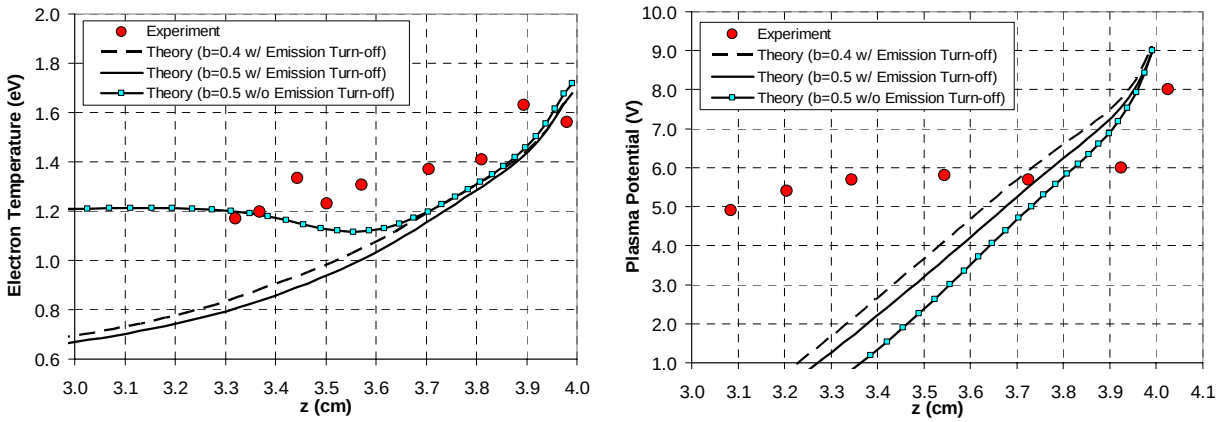

Fig 15. Comparison between measurements and theory (using the IROrCa2D code) along the axis of symmetry of the NSTAR cathode, including theory cases of emission turn-off at negative potential. Left: Electron temperature. Right: Plasma potential.

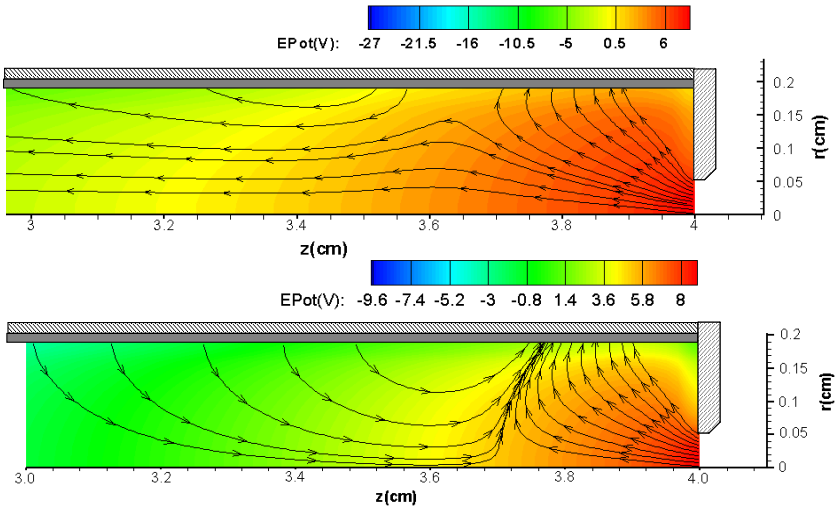

Fig 16. Computed 2D profiles of the plasma potential in the NSTAR cathode for the case of b=0.5, overlaid by electron current density streamlines. Top: Emission turn-off not applied. Bottom: Emission turn-off applied.

B. Simulation of the NEXIS Cathode with OrCa2D

Even though OrCa2D is a descendent of IROrCa2D, the several augmentations in physics and numerics described above effectively make OrCa2D a new code. Validation of OrCa2D would require that it re-produces the agreement with experimental measurements achieved by IROrCa2D in the emitter region at the same total pressure, if the latter is indeed uniform throughout the region. Figure 18 shows the total pressure as computed by OrCa2D and Fig 18 (left) shows its variation along the axis of symmetry at t≈3ms. The average pressure in the emitter region, up to z=4cm, is 1.03T and the deviation from this average does not exceed 1.5%. Figure 18 (right) shows that the pressure continues to decrease beyond 3ms, and is due to the absence of physical models that involve ion acceleration and viscosity. We plan to include the missing physical models in OrCa2D in the near future.

Figure 19 shows a comparison of the plasma density, electron temperature and plasma potential variation along the centerline as computed by IROrCa2D and OrCa2D at the same total pressure. The computed 2D profiles of these variables are also depicted in Fig 20-Fig 22. All three variables are found to be in close agreement. Figure 23 shows the electron current density streamlines. It is noted that no emission enhancement (b=0) has been employed in these simulations. The neutral particle density and peak heavy-species temperature solutions are shown in Fig 24 and Fig 25, respectively. The heavy-species temperature is found to be approximately 400 K higher than the IROrCa2D result which is due to the higher relative velocities between ions and neutrals. It is recalled that IROrCa2D assumes u_n=0 everywhere in the emitter region. OrCa2D computes velocities in the order of a few hundred meters per second near the orifice entrance (z<4cm).

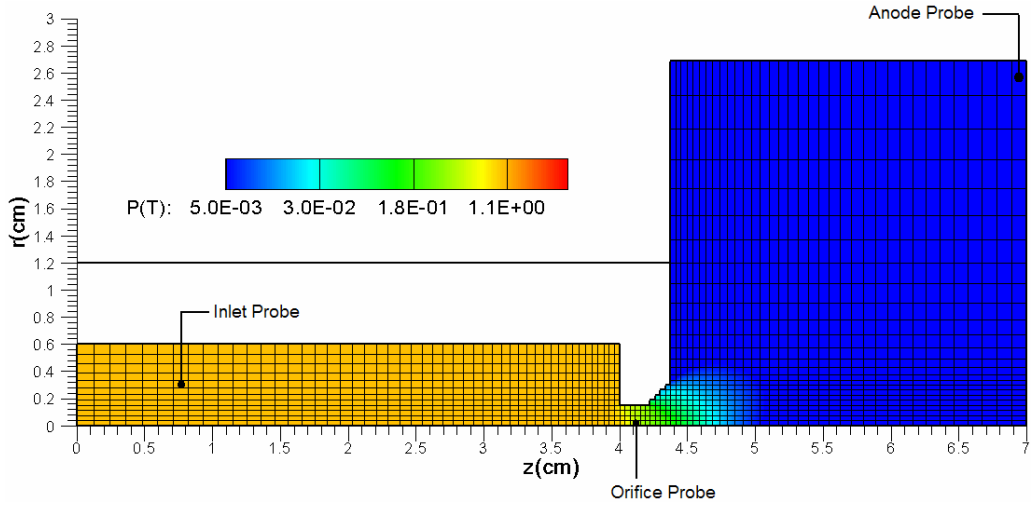

Fig 17. 2D profile of the total pressure inside and outside the NEXIS cathode computed by OrCa2D at t=3ms.

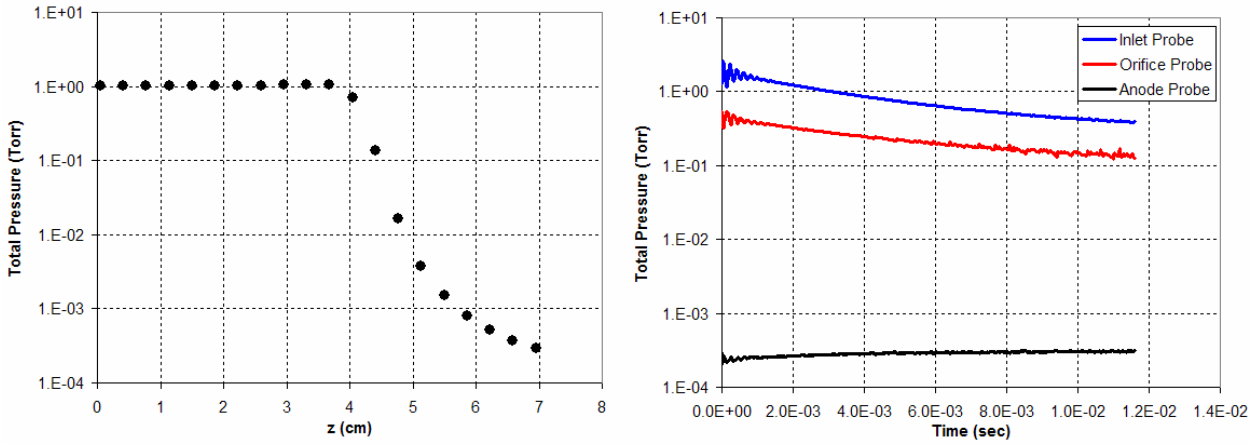

Fig 18. Total pressure computed by OrCa2D. Left: Along axis of symmetry at t=3ms. Right: As a function of time at three locations.

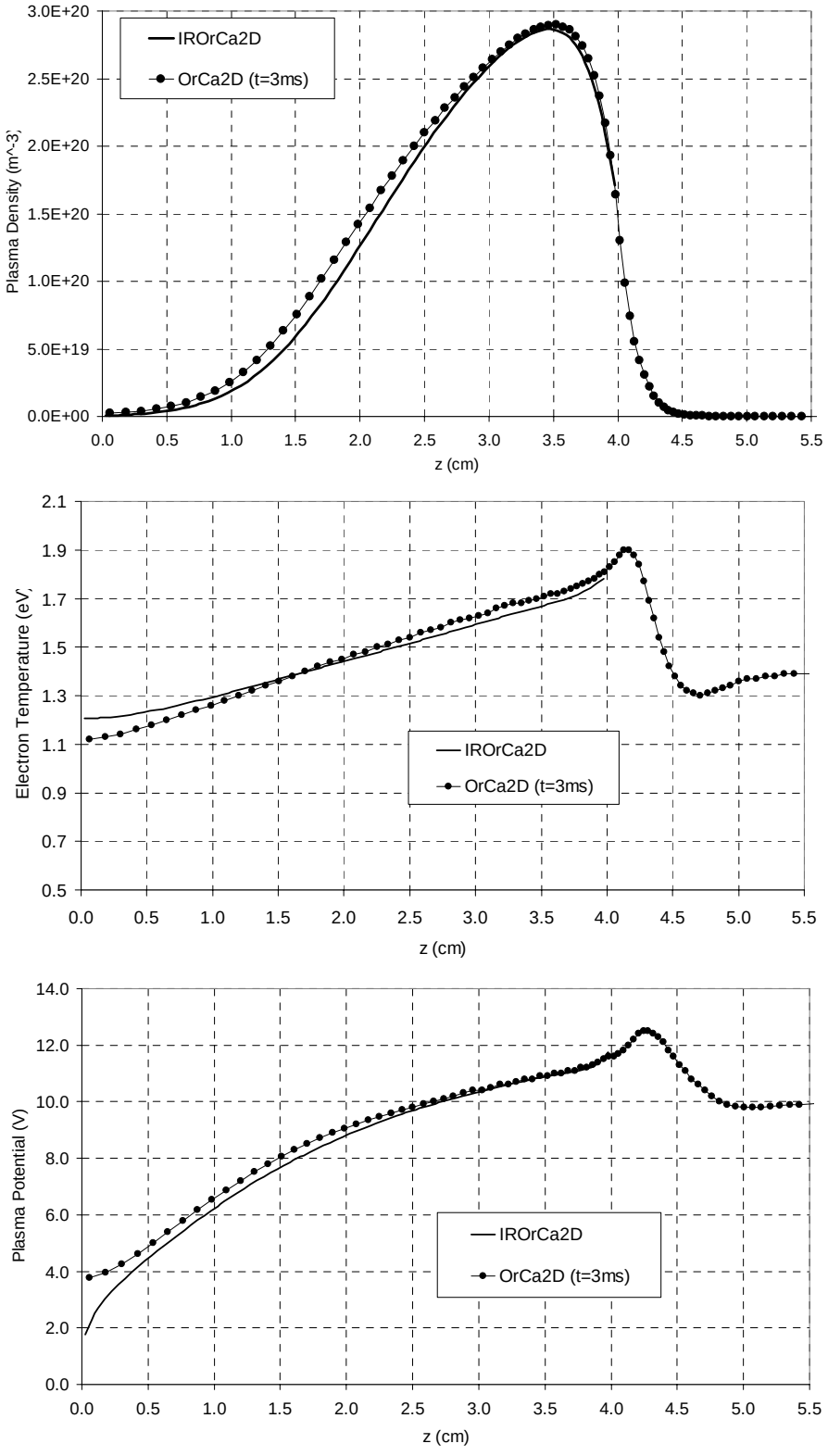

Fig 19. Comparisons between the IROrCa2D steady-state solution (P=1T) and the OrCa2D solution at t=3ms.

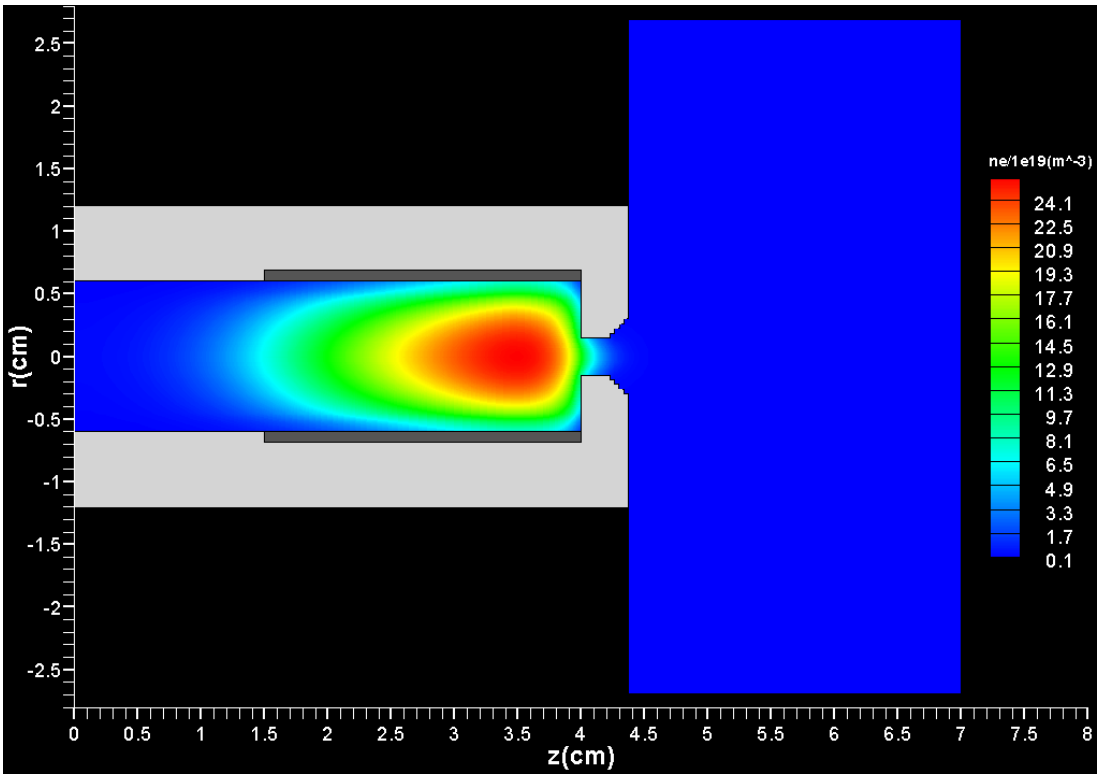

Fig 20. Plasma particle density contours in the NEXIS cathode and plume regions (t=3ms).

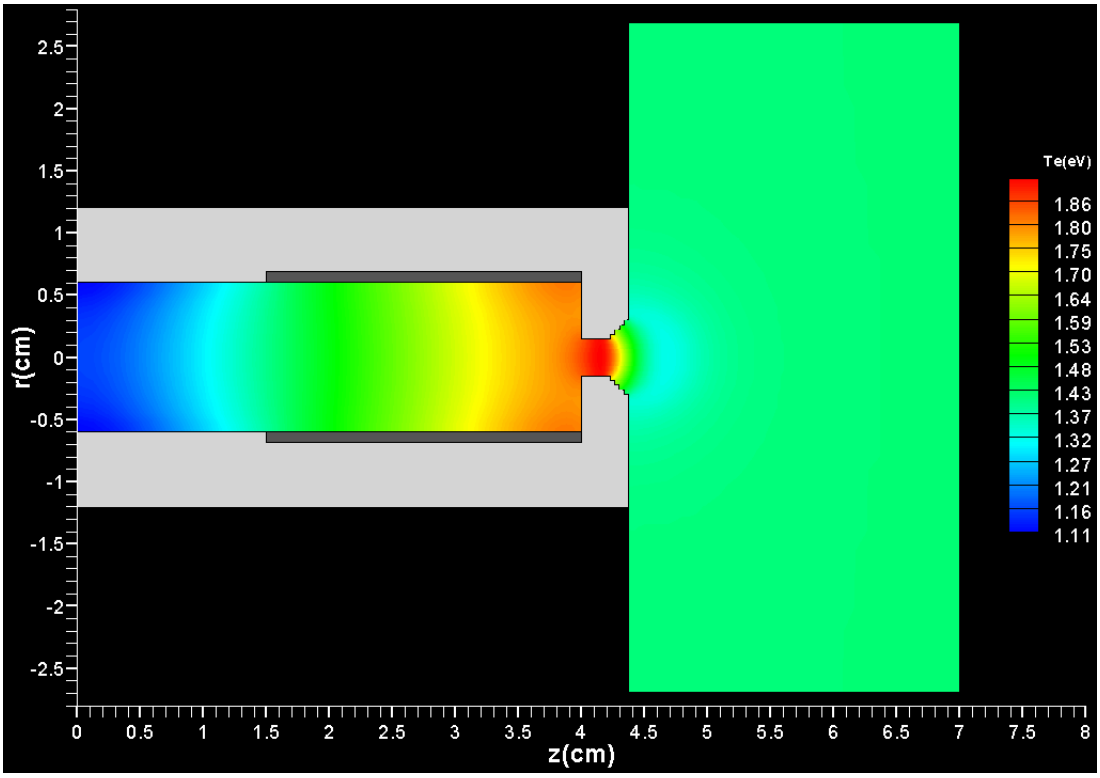

Fig 21. Electron temperature contours in the NEXIS cathode and plume regions (t=3ms).

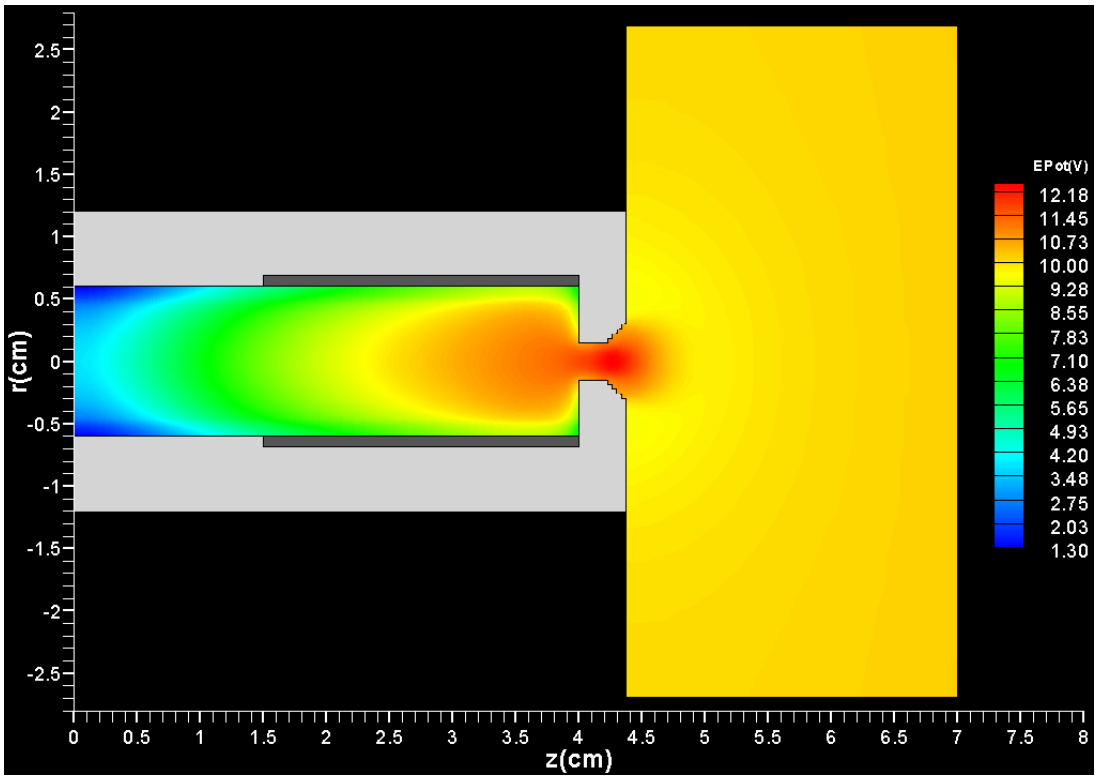

Fig 22. Plasma potential contours in the NEXIS cathode and plume regions (t=3ms).

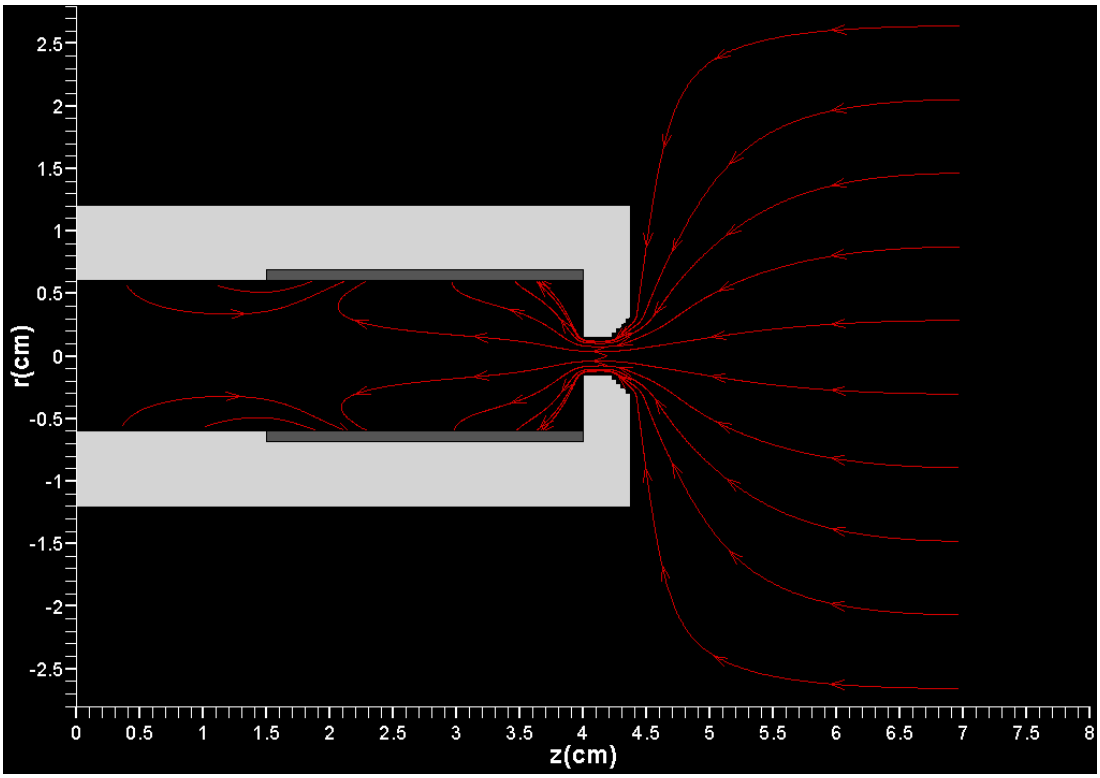

Fig 23. Electron current density streamlines in the NEXIS cathode and plume regions (t=3ms).

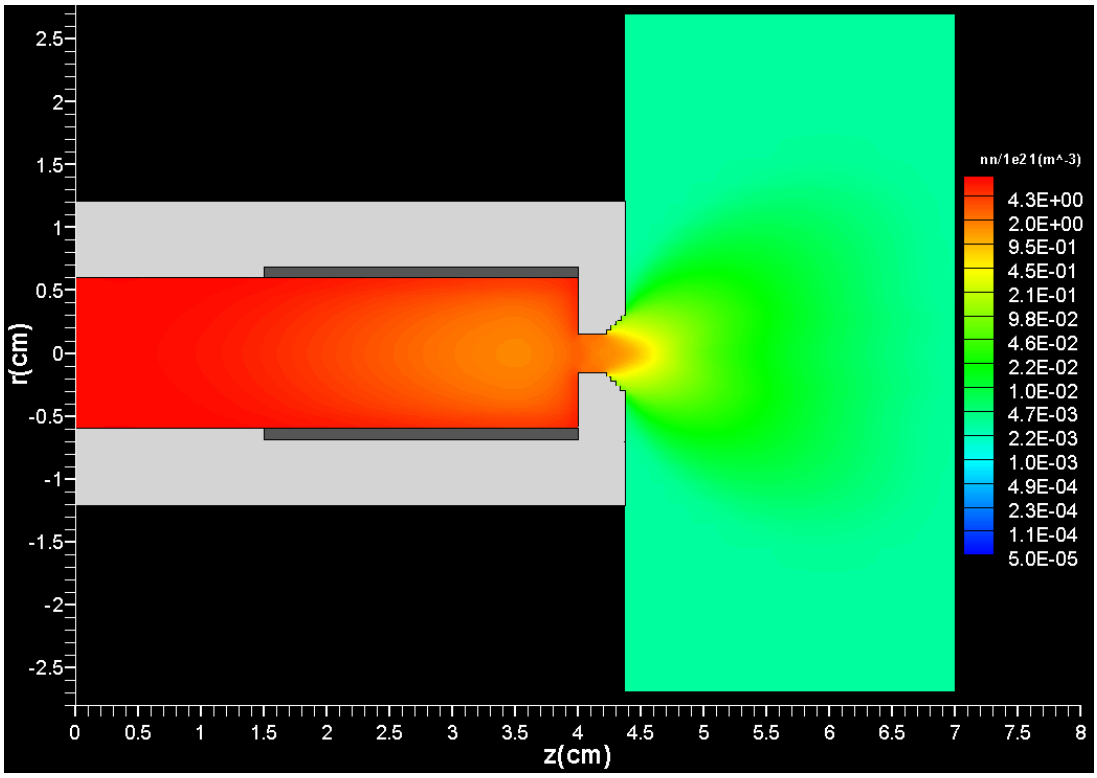

Fig 24. Neutral particle density contours in the NEXIS cathode and plume regions (t=3ms).

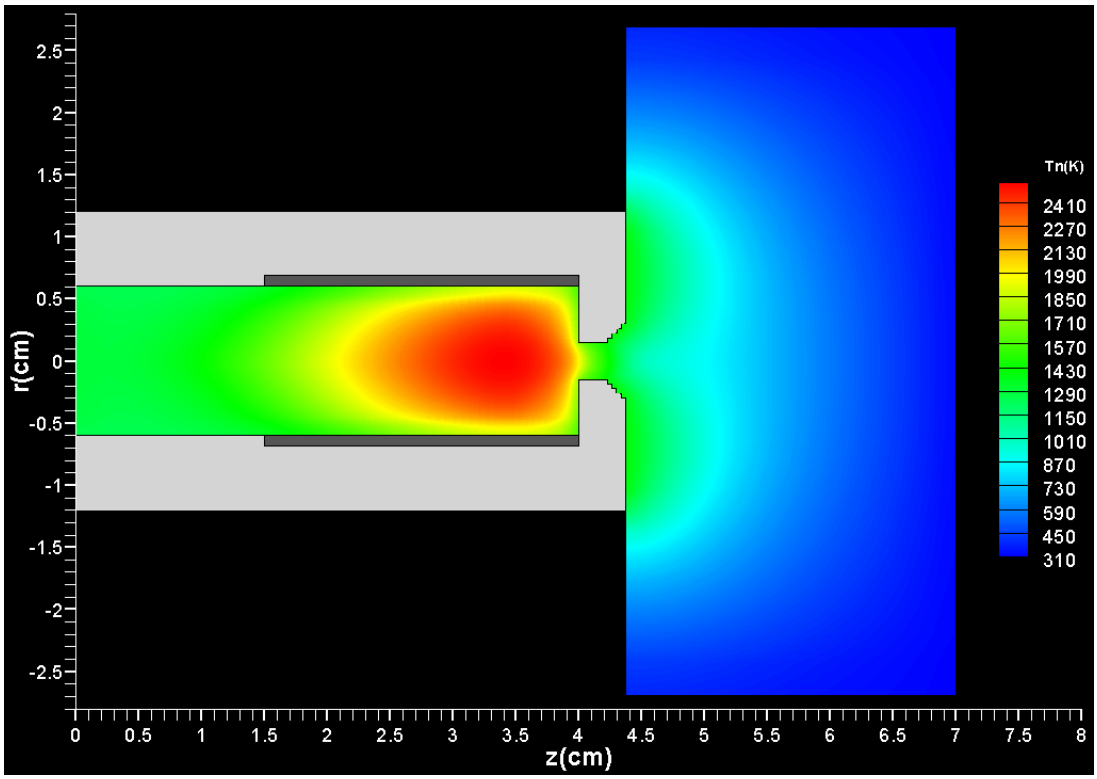

Fig 25. Heavy-species temperature contours in the NEXIS cathode and plume regions (t=3ms).

The far-plume ($z \geq \sim 5$cm) region is found to be relatively benign and the choice of the plasma density boundary condition at the anode is found to affect negligibly the solution in the near-plume region. Figure 26 shows the relevant mean free paths (MFPs) along the axis of symmetry in the orifice and plume regions. The NEXIS cathode orifice diameter is 3mm and the exit diameter at the end of the conical section (z=4.375 cm) is 6mm. Figure 26 suggests that the collisionality of the electron fluid is retained mostly due to e-i Coulomb collisions in the orifice region. In this region ion-neutral collisions occur at least once to a few times before ions are lost to the walls. Neutral-neutral collisions are less frequent but the Knudsen number is in the order of unity for which the solution to the fluid equations will not deviate substantially from the true solution.

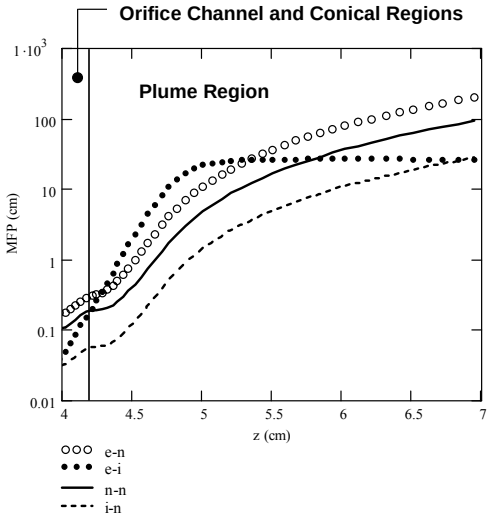

Fig 26. Collision mean free paths calculated in the orifice and plume regions of the simulated NEXIS cathode (orifice channel diameter=0.3 cm, orifice conical section max diameter=0.6 cm).

The measurement depicted in Fig 27 shows that both the plasma potential and electron temperature continue to increase beyond the cathode exit. The trend is not predicted by the classical calculation of OrCa2D. Mikellides *et al*.[8] suggested that anomalous heating near the orifice region may occur as a result of two-stream instabilities. The reason for the proposition can easily be explained once again by eqn (26). In the coordinate system chosen in this paper, as electrons expand downstream of the orifice exit the electron pressure decreases and the pressure gradient force is negative. The electron current density is also negative as electrons are extracted from the orifice in the +z direction and the resistive term in eqn (26) is therefore positive. For the plasma potential to establish a positive slope in the region the resistive term must prevail over the pressure gradient force (again assuming that the contribution of the ion current is negligible). Calculations using classical transport indicate that although sufficient current density is drawn to satisfy the total current condition the computed potential gradient does not exhibit the measured trend. Thus, in view of the high electron drifts computed in the near-plume region enhanced resistance is a possible explanation for the observed trend.

During the NEXIS simulations with IROrCa2D last year it was determined that up to the orifice entrance the electron Mach number M_e defined as the ratio of the relative e-i drift velocity over $(kT_e/m_e)^{1/2}$ was less than about 0.2. As a consequence only weak turbulence by ion-acoustic waves was proposed as the probable source of anomalous heating, with an effective anomalous collision frequency first proposed by Sagdeev[13] (also in Hamberger and Friedman[14]) as follows:

$$\nu_{anom} \approx 10^{-2} \frac{\sqrt{\pi}}{8} \frac{T_e}{T_i} \frac{u_d}{\bar{c}_e} \omega_e \tag{27}$$

The result of including Sagdeev's anomalous frequency in IROrCa2D is repeated in Fig 27 for comparison. The IROrCa2D calculation also showed an increasing M_e with z but it was not possible to determine the behavior of M_e beyond the orifice entrance.

Using classical transport only, Fig 28 (left) shows the profile of M_e beyond the orifice entrance as computed by OrCa2D. It is now seen that M_e not only exceeds unity but it reaches values as high as seven in the near plume region. Buneman[15] (1959) showed that in this case it is possible to excite waves that have rapid growth rates, and are considerably more turbulent than ion-acoustic oscillations. Specifically, the Buneman wave frequency ω_B is,

$$\omega_B \approx \left(\frac{m_e}{16m}\right)^{1/3} \omega_e \tag{28}$$

where ω_e is the electron plasma frequency. An effective anomalous collision frequency has been proposed by several authors and differs from the above by the (m_e/m) exponent. For example, Hamberger and Friedman[14] use 1/3 while other authors propose different exponents.[16,17] For comparison purposes eqn (28) above is taken to be the representative anomalous collision frequency as we compare the increase in the plasma resistivity due to Buneman and due to Sagdeev (eqn (27)). It is seen in Fig 28 that the enhancement can be as high as 50 times under conditions that satisfy the Buneman criterion, which could lead to significantly more heating of the electrons than the weak turbulence represented by Sagdeev's collision frequency. In view of the violent nature (short lifetime) of the Buneman instability, A. Treumann proposes that its effect is to "prepare" the plasma to become ion-acoustic wave unstable by heating it to electron temperatures higher than the ion temperature, which would explain the recent ion-acoustic type of oscillations measured in the near-plume region of the hollow cathode.[5] As part of our near-future investigations with OrCa2D all of the above will be investigated. All OrCa2D results presented thus far have not employed anomalous resistivity.

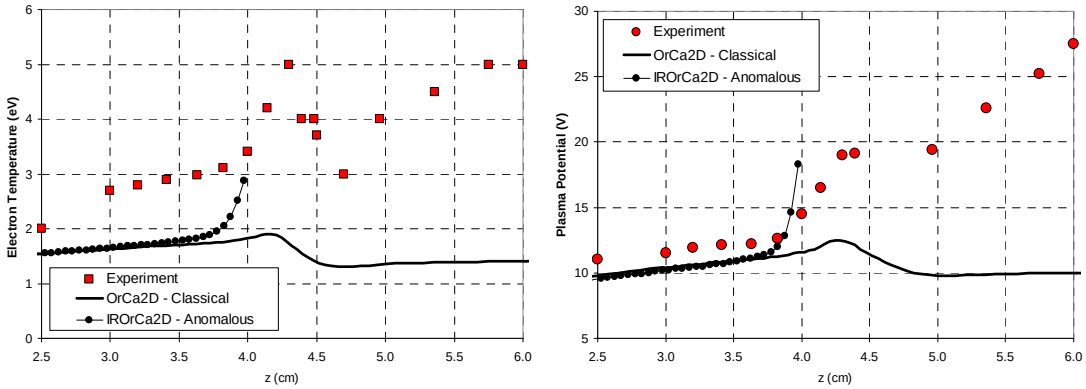

Fig 27. Comparison between measured and calculated values along the axis of symmetry of the NEXIS cathode. The IROrCa2D results include anomalous resistivity using Sagdeev's eqn (27).
Left: Electron temperature. Right: Plasma Potential.

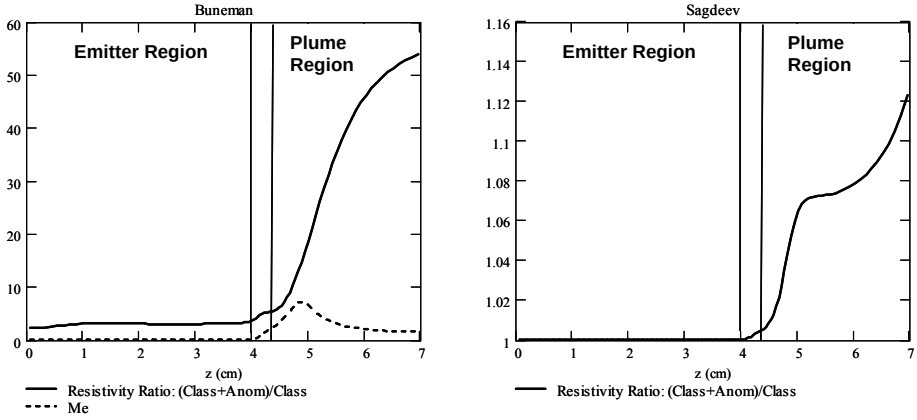

Fig 28. Calculated resistivity enhancement. Left: Using Buneman's wave frequency as the effective anomalous collision frequency. Right: Using Sagdeev's anomalous collision frequency for weak ion-acoustic turbulence.

IV. Conclusion

The simulations of the NSTAR cathode emitter region with IROrCa2D suggest that emission is enhanced as the sheath along the insert becomes small enough to allow sheath penetration into the emitter pores thereby increasing the effective emission area. The sheath size is reduced in the NSTAR cathode because it operates at much higher plasma densities (peak~10^{21} m^{-3}) than the NEXIS cathode (peak~10^{20} m^{-3}). The latter has been simulated as a 1.2cm-diameter channel with a 3-mm orifice diameter operating nominally at 5.5sccm and 25A. The NSTAR cathode has been simulated to have a 4-mm channel diameter and 1mm orifice diameter with nominal operating condition of 4.2sccm and 12A (it is recalled that it is the inner diameter of the insert that defines the computational region in the simulations, not the channel tube diameter). *Without* emission enhancement the simulations suggest that the emitter would be utilized to a larger extent than the few millimeters presently shown by the simulations *with* enhancement.

Simulations of the NEXIS cathode with the time-dependent code OrCa2D show that the resistive contribution to the electric field in the near-plume region is not sufficiently larger (in magnitude) than the electron pressure gradient force to induce the monotonically increasing plasma potential measured in the experiment. It is postulated that enhanced resistance as a result of two-streaming instabilities may be responsible for the observed trend. The hypothesis is based on the high e-i relative drifts calculated by OrCa2D in the near-plume region using classical transport and the observed plasma oscillations captured in recent experiments.

Acknowledgments

The research described in this paper was carried out by the Jet Propulsion Laboratory, California Institute of Technology, under a contract with the National Aeronautics and Space Administration for the Prometheus Advanced Systems and Technology Office.

References

[1] A. Sengupta, J. R. Brophy, and K. D. Goodfellow, AIAA Paper 03-4558, 39th AIAA/ASME/SAE/ASEE Joint Propulsion Conference, Huntsville, Alabama, 2003.
[2] A. Sengupta, *et al*., NASA T/TP 2004-213391, (2004).
[3] D. E. Siegfried and P. J. Wilbur, AIAA Paper 78-705, 13th AIAA/DGLR International Electric Propulsion Conference, San Diego, California, 1978.
[4] D.M. Goebel, A. Sengupta, A. Watkins, K. Jameson, AIAA Paper 04-3430, 40th AIAA/ASME/SAE/ASEE Joint Propulsion Conference, Fort Lauderdale, Florida, 2004.
[5] K. Jameson and D. Goebel, AIAA Paper 05-3667, 41st AIAA/ASME/SAE/ASEE Joint Propulsion Conference, Tucson, Arizona, 2005.
[6] I. Kameyama and P.J. Wilbur, ISTS Paper 98-a-2-18, 21st International Symposium on Space Technology and Science, Omiya, 1998.
[7] I. Kameyama, NASA Contractor Report 204154 (1997).
[8] I.G. Mikellides, I. Katz, D. Goebel and J. Polk, AIAA Paper 04-3817, 40th AIAA/ASME/SAE/ASEE Joint Propulsion Conference, Fort Lauderdale, Florida, 2004. (Updated version also submitted to the *Journal of Applied Physics*).
[9] S. Dushman, Phys. Rev., **21**, 623 (1923).
[10] J. E. Polk, C. Marrese, B. Thornber, L. Dang and L. Johnson, AIAA Paper 04-4116, 40th AIAA/ASME/SAE/ASEE Joint Propulsion Conference, Fort Lauderdale, Florida, 2004
[11] J. L. Cronin, in IEEE Proceedings **128**, 1, pp. 19-32, (1981).
[12] R.T. Longo, private communication.
[13] R. Z. Sagdeev, in *Proceedings of the 18th Symposium in Applied Mathematics*, 1967, p. 281.
[14] S. M. Hamberger and M. Friedman, Phys. Rev., **21**, 674 (1968).
[15] O. Buneman, Phys. Rev., **115**, 503 (1959).
[16] R. A. Treumann, Earth Planet Space, **53**, pp. 453-462 (2001).
[17] A. Hirose, Plasma Physics, 20, pp. 481-485, (1978)